01 Sep 2010

Baryon Acoustic Oscillations in 2D: Modeling Redshift-Space Power Spectrum from Perturbation Theory

Atsushi Taruya

Takahiro Nishimichi

Shun Saito
Missouri University of Science and Technology, saitos@mst.edu

Recommended Citation

A. Taruya et al., "Baryon Acoustic Oscillations in 2D: Modeling Redshift-Space Power Spectrum from Perturbation Theory," *Physical Review D - Particles, Fields, Gravitation and Cosmology*, vol. 82, no. 6, American Physical Society (APS), Sep 2010.
The definitive version is available at https://doi.org/10.1103/PhysRevD.82.063522

PHYSICAL REVIEW D **82,** 063522 (2010)

Baryon acoustic oscillations in 2D: Modeling redshift-space power spectrum from perturbation theory

Atsushi Taruya,[1,2] Takahiro Nishimichi,[2] and Shun Saito[3,4]

[1]*Research Center for the Early Universe, School of Science, The University of Tokyo, Bunkyo-ku, Tokyo 113-0033, Japan*
[2]*Institute for the Physics and Mathematics of the Universe, University of Tokyo, Kashiwa, Chiba 277-8568, Japan*
[3]*Department of Physics, The University of Tokyo, Bunkyo-ku, 113-0033, Japan*
[4]*Department of Astronomy, 561-A Campbell Hall, University of California, Berkeley, California 94720, USA*
(Received 11 June 2010; published 16 September 2010)

We present an improved prescription for the matter power spectrum in redshift space taking proper account of both nonlinear gravitational clustering and redshift distortion, which are of particular importance for accurately modeling baryon acoustic oscillations (BAOs). Contrary to the models of redshift distortion phenomenologically introduced but frequently used in the literature, the new model includes the corrections arising from the nonlinear coupling between the density and velocity fields associated with two competitive effects of redshift distortion, i.e., Kaiser and Finger-of-God effects. Based on the improved treatment of perturbation theory for gravitational clustering, we compare our model predictions with the monopole and quadrupole power spectra of N-body simulations, and an excellent agreement is achieved over the scales of BAOs. Potential impacts on constraining dark energy and modified gravity from the redshift-space power spectrum are also investigated based on the Fisher-matrix formalism, particularly focusing on the measurements of the Hubble parameter, angular diameter distance, and growth rate for structure formation. We find that the existing phenomenological models of redshift distortion produce a systematic error on measurements of the angular diameter distance and Hubble parameter by 1%–2% , and the growth-rate parameter by ~5%, which would become non-negligible for future galaxy surveys. Correctly modeling redshift distortion is thus essential, and the new prescription for the redshift-space power spectrum including the nonlinear corrections can be used as an accurate theoretical template for anisotropic BAOs.

DOI: 10.1103/PhysRevD.82.063522 PACS numbers: 98.80.−k, 95.36.+x, 98.65.−r

I. INTRODUCTION

Galaxy redshift surveys via the spectroscopic measurements of individual galaxies provide a three-dimensional map of the galaxy distribution, which includes valuable cosmological information on structure formation of the Universe. The observed galaxy distribution is, however, apparently distorted due to the peculiar velocity of galaxies that systematically affects the redshift determination of each galaxy. The anisotropy caused by peculiar velocities is referred to as the *redshift distortion*, which complicates the interpretation of the galaxy clustering data (e.g., [1,2]).

Nevertheless, redshift distortion provides a unique way to measure the growth rate of structure formation, which has been previously used for determining the density parameters of the Universe (e.g., [3,4]), and is now recognized with great interest as a powerful tool for testing gravity on cosmological scales (e.g., [5–9]). Redshift distortion also provides helpful information on the dark-sector interactions [10], where the dark energy is dynamically coupled with dark matter (e.g., [11,12]). Note that the distortion of the galaxy clustering pattern also arises from the apparent mismatch of the underlying cosmology when we convert the redshift and angular position of each galaxy to the comoving radial and transverse distances. This is known as the Alcock-Paczynski effect [13], and with the baryon acoustic oscillations (BAOs) as a robust standard ruler, it can be utilized for a simultaneous measurement of the Hubble parameter $H(z)$ and angular diameter distance $D_A(z)$ of distant galaxies at redshift z (e.g., [14–18]).

In these respects, anisotropic clustering data from galaxy redshift surveys serve as a dual cosmological probe of cosmic expansion and gravity on cosmological scales, from which we can address properties of both the dark energy and modification of gravity responsible for the late-time cosmic acceleration. Although current data are not yet sensitive enough to simultaneously measure $H(z)$, $D_A(z)$ and the growth rate (see [7,19–21] for current status), planned and ongoing galaxy redshift surveys aim at precisely measuring the anisotropic power spectrum and/or two-point correlation function in redshift space. Thus, accurate theoretical modeling of the anisotropic power spectrum is crucial and needs to be developed toward future observations.

The purpose of this paper is to address these issues based on the analytical treatment of nonlinear gravitational clustering. In the single-stream limit, cosmological evolution of the mass distribution consisting of cold dark matter and baryons is described by the coupled equations for an

irrotational and pressureless fluid [22]. Recently, a detailed study on the standard treatments of perturbation theory has been made [23–25], and several improved treatments have been proposed [26–38], showing that percent-level accuracy can be achieved for predictions of the power spectrum or two-point correlation function in real space, over the scales of interest for BAOs; for instance, at $z = 1$, the predictions are well converged to the N-body results at $k \lesssim 0.23h$ Mpc^{-1} for the power spectrum [34]. With the help of these methods, in this paper, we will develop a model of redshift distortion, and compute the matter power spectrum in redshift space, with particular attention paid to the BAOs. We also discuss the impact of model uncertainty of the redshift distortion on the acoustic-scale measurement of BAOs and the estimation of the growth-rate parameter.

This paper is organized as follows: In Sec. II, we start by writing down the relation between real space and redshift space, and derive an exact expression for the matter power spectrum in redshift space. We then consider the existing theoretical models of redshift distortion, and compare those with N-body simulations in Sec. III, showing that non-negligible discrepancy appears at the scales of BAOs. In Sec. IV, nonlinear corrections relevant to describe the small discrepancies are derived based on the exact expression for the redshift-space power spectrum. The new model of redshift distortion including the corrections reproduces the N-body simulations quite well in both the monopole and quadrupole components of the redshift-space power spectrum. In Sec. V, the relevance of this new model is discussed in detail, especially for measurements of acoustic scales and growth-rate parameters. The potential impact of the model of redshift distortion on future constraints for modified gravity and dark energy is also estimated based on the Fisher-matrix formalism. Finally, our important findings are summarized in Sec. VI.

Throughout the paper, we assume a flat ΛCDM model and adopt the fiducial cosmological parameters based on the five-year WMAP results [39]: $\Omega_{\rm m} = 0.279$, $\Omega_\Lambda = 0.721$, $\Omega_{\rm b}/\Omega_{\rm m} = 0.165$, $h = 0.701$, $n_s = 0.96$, and $\sigma_8 = 0.817$. In order to compare our analytic results with N-body simulations, the data are taken from Ref. [34], in which 30 independent N-body simulations of 512^3 particles and cubic boxes of side length $1h^{-1}$ Gpc were carried out with initial conditions created by the 2LPT code [40] at $z_{\rm init} = 31$, adopting the same cosmological parameters as mentioned above. The output data were stored at redshifts $z = 3$, 2, 1, and 0.5, and were created by a publicly available cosmological N-body code, GADGET2 [41], with softening length of $0.1h^{-1}$ Mpc for tree forces. Convergence checks of the N-body code adopting the simulation parameters mentioned here have been previously investigated in detail in Ref. [25], and we believe that the N-body results in this paper are accurate enough to discuss a percent-level precision, at least on the scales of BAOs.

II. POWER SPECTRUM IN REDSHIFT SPACE

Let us first recall that the redshift distortion arises from the apparent mismatch of galaxy positions between real and redshift spaces caused by the contamination of the peculiar velocities in the redshift measurement. For distant galaxies, the position in real space, $\boldsymbol{r}$, is mapped to the one in redshift space, $\boldsymbol{s}$, as

$$\boldsymbol{s} = \boldsymbol{r} + \frac{v_z(\boldsymbol{r})}{aH(z)}\hat{\boldsymbol{z}}, \tag{1}$$

where the unit vector $\hat{\boldsymbol{z}}$ indicates the line-of-sight direction, and quantity v_z is the line-of-sight component of the velocity field, i.e., $v_z = \boldsymbol{v}\cdot\hat{\boldsymbol{z}}$. The quantities a and H are the scale factor of the Universe and the Hubble parameter, respectively. Then, the density field in redshift space, $\delta^{(\rm S)}(\boldsymbol{s})$, is related to the one in real space, $\delta(\boldsymbol{r})$ through the relation $\{1 + \delta^{(\rm S)}(\boldsymbol{s})\}d^3\boldsymbol{s} = \{1 + \delta(\boldsymbol{r})\}d^3\boldsymbol{r}$, which leads to

$$\delta^{(\rm S)}(\boldsymbol{s}) = \left|\frac{\partial \boldsymbol{s}}{\partial \boldsymbol{r}}\right|^{-1}\{1 + \delta(\boldsymbol{r})\} - 1. \tag{2}$$

The Fourier transform of this is given by

$$\delta^{(\rm S)}(\boldsymbol{k}) = \int d^3\boldsymbol{r}\left\{\delta(\boldsymbol{r}) - \frac{\nabla_z v_z(\boldsymbol{r})}{aH(z)}\right\}e^{i(k\mu v_z/H + \boldsymbol{k}\cdot\boldsymbol{r})}, \tag{3}$$

where the quantity μ is the cosine of the angle between $\hat{z}$ and $\boldsymbol{k}$. Here, we used the fact that the Jacobian $|\partial\boldsymbol{s}/\partial\boldsymbol{r}|$ is written as $1 + \nabla_z v_z/(aH)$.

From this, the power spectrum of the density field in redshift space becomes [42]

$$P^{(\rm S)}(\boldsymbol{k}) = \int d^3\boldsymbol{x} e^{i\boldsymbol{k}\cdot\boldsymbol{x}}\langle e^{-ik\mu f\Delta u_z}\{\delta(\boldsymbol{r}) + f\nabla_z u_z(\boldsymbol{r})\} \times \{\delta(\boldsymbol{r}') + f\nabla_z u_z(\boldsymbol{r}')\}\rangle, \tag{4}$$

where $\boldsymbol{x} = \boldsymbol{r} - \boldsymbol{r}'$ and $\langle\cdots\rangle$ denotes an ensemble average. We defined $u_z(\boldsymbol{r}) = -v_z(\boldsymbol{r})/(aHf)$ and $\Delta u_z = u_z(\boldsymbol{r}) - u_z(\boldsymbol{r}')$. The function f is the logarithmic derivative of the linear growth function $D(z)$ given by $f = d\ln D(z)/d\ln a$. This is the exact expression for the power spectrum in redshift space, and no dynamical information for velocity and density fields, i.e., the Euler equation and/or continuity equation, is invoked in deriving this equation.

In the expression (4), the power spectrum is written as a function of k and μ, and is related to the statistical average of real-space quantities in a complicated manner, but qualitative effects on the clustering amplitude of the power spectrum are rather clear, i.e., enhancement and damping, well known as the Kaiser and Finger-of-God effects [43–45]. The Kaiser effect basically comes from the braces on the right-hand side of the expression (4), which represents the coherent distortion by the peculiar velocity along the line-of-sight direction. In linear theory, the relation $u = \delta$ holds and the strength of clustering anisotropies is controlled by the growth-rate parameter f. This is the basic reason why the redshift distortion attracts much attention as a powerful indicator for growth of structure. On the

other hand, the Finger-of-God effect roughly comes from the factor $e^{-ik\mu f\Delta u_z}$ in Eq. (4). Because of the randomness of peculiar velocities, dephasing arises which leads to the suppression of clustering amplitude. The apparent reduction of amplitude becomes especially significant around the halo forming regions.

Of course, these two effects cannot be separately treated in principle, and a mixture of Kaiser and Finger-of-God effects is expected to be significant in the translinear regime, where a tight correlation between velocity and density fields still remains. This is of particular importance for the accurate modeling of BAOs. Before addressing detailed modeling, however, we will first consider currently existing models of redshift distortion, and examine how these models fail to reproduce the major trends of BAO features in redshift space.

III. EXISTING MODELS OF REDSHIFT DISTORTION

A. Perturbation theory description

Let us first examine the perturbation theory (PT) based model of redshift distortion. We here specifically deal with the two representative models: one-loop PT calculations for redshift-space power spectrum from standard PT and Lagrangian PT.

The standard PT usually implies a straightforward expansion of the cosmic fluid equations around their linear solution, assuming that the amplitudes of density and velocity fields are small. This treatment is also applied to the evaluation of redshift-space power spectrum (4), and the resultant expressions for the one-loop power spectrum are schematically summarized as (see [29,46] for complete expressions)

$$P^{(\mathrm{S})}_{\mathrm{SPT}}(k,\mu) = (1+f\mu^2)^2 P_{\mathrm{lin}}(k) + P^{(\mathrm{S})}_{\text{1-loop}}(k,\mu). \quad (5)$$

The first term on the right-hand side is the linear-order result of the redshift-space power spectrum, and the factor $(1+f\mu^2)^2$ multiplied by the linear power spectrum P_{lin} indicates the enhancement due to the Kaiser effect. The second term $P^{(\mathrm{S})}_{\text{1-loop}}$ represents a collection of the leading-order mode-coupling terms called one-loop corrections, arising both from the gravitational clustering and the redshift distortion. This term is basically of the fourth order in linear-order density or velocity fields, and is roughly proportional to $P_{\mathrm{lin}}\Delta^2$ with $\Delta^2 = k^3 P_{\mathrm{lin}}/(2\pi^2)$.

On the other hand, the Lagrangian PT description of the redshift-space power spectrum is obtained in a somewhat different way. Intuitively, we rewrite the exact expression (4) in terms of the displacement vector, and the perturbative expansion is applied to the displacement vector. Although a naive perturbative treatment merely reproduces the standard PT result (5), Ref. [29] has applied a partial expansion, and some of the terms have been kept in some nonperturbative ways. The resultant expression for the power spectrum in redshift space becomes

$$P^{(\mathrm{S})}_{\mathrm{LPT}}(k,\mu) = e^{-k^2\{1+f(f+2)\mu^2\}\sigma^2_{\mathrm{v,lin}}} \times [P^{(S)}_{\mathrm{SPT}}(k,\mu) + (1+f\mu^2)^2 \times \{1+f(f+2)\mu^2\}k^2\sigma^2_{\mathrm{v,lin}}], \quad (6)$$

where the quantity $\sigma^2_{\mathrm{v,lin}}$ is the linear-order estimate of the one-dimensional velocity dispersion given by

$$\sigma^2_{\mathrm{v,lin}} = \frac{1}{3}\int \frac{d^3\boldsymbol{q}}{(2\pi)^3}\frac{P_{\mathrm{lin}}(q,z)}{q^2}. \quad (7)$$

The exponential prefactor in Eq. (6) can be regarded as the result of nonperturbative treatment, and in redshift space, this term accounts for the nonlinear damping of the BAOs arising both from the gravitational clustering and Finger-of-God effect of redshift distortion.

Figure 1 compares the PT-based models of redshift distortion with the N-body simulations of Ref. [34]. The left and right panels, respectively, show the monopole ($\ell = 0$) and quadrupole ($\ell = 2$) moments of the power spectrum divided by the smooth reference spectrum at different redshifts, $z = 3$, 1, and 0.5 (from top to bottom). The reference spectrum $P^{(\mathrm{S})}_{\ell,\text{no-wiggle}}(k)$ is calculated from the no-wiggle approximation of the linear transfer function in Ref. [47], taking account of the linear-order result of the Kaiser effect. The multipole moments of the two-dimensional power spectrum are defined by

$$P^{(\mathrm{S})}_{\ell}(k) = \frac{2\ell+1}{2}\int_{-1}^{1} d\mu P^{(\mathrm{S})}(k,\mu)\mathcal{P}_\ell(\mu), \quad (8)$$

with $\mathcal{P}_\ell(\mu)$ denoting the Legendre polynomials.

As has been repeatedly stated in the literature [23,25,34,48], the standard PT treatment is not sufficiently accurate to describe the BAOs. Figure 1 confirms that this is indeed true not only in real space, but also in redshift space. While the power spectrum amplitude of N-body simulations tends to be smaller than that of the linear-theory prediction (dotted lines), the predicted amplitude of standard PT generally overestimates the N-body results, and it exceeds the linear prediction on small scales. Compared to the results in real space, the discrepancy between prediction and simulation seems a bit large. For instance, at $z = 1$, the standard PT prediction for the monopole spectrum starts to deviate from the N-body results at $k \sim 0.07h$ Mpc^{-1}, whereas a good agreement between prediction and N-body simulation still holds at $k \lesssim 0.13h$ Mpc^{-1} in real space (see vertical arrows in Fig. 5). In contrast, in the Lagrangian PT calculation, the amplitude of the power spectrum is rather suppressed, and a better agreement between prediction and simulation is achieved at low k. This is due to the exponential prefactor in Eq. (6). As a trade-off, however, the predicted amplitude at higher k modes largely underestimates the result of N-body simulations. Further, a closer look at the first

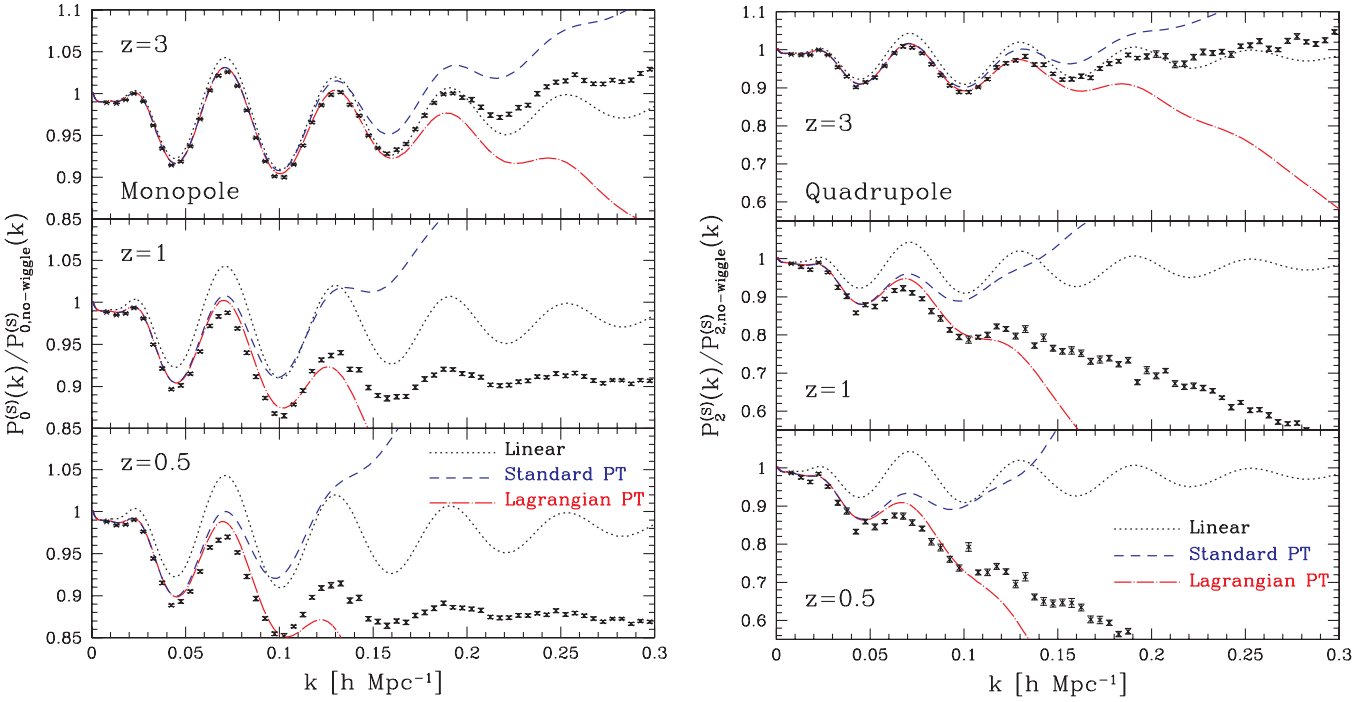

FIG. 1 (color online). Ratio of power spectra to smoothed reference spectra in redshift space, $P_\ell^{(S)}(k)/P_{\ell,\mathrm{no\text{-}wiggle}}^{(S)}(k)$. N-body results are taken from the WMAP5 simulations of Ref. [34]. The reference spectrum $P_{\ell,\mathrm{no\text{-}wiggle}}^{(S)}$ is calculated from the no-wiggle approximation of the linear transfer function with the linear theory of the Kaiser effect taken into account. Short dashed and dot-dashed lines, respectively, indicate the results of one-loop PT and Lagrangian PT calculations for the redshift-space power spectrum [Eqs. (5) and (6)].

peak of BAOs around $k \sim 0.05 - 0.1h$ Mpc^{-1} reveals a small discrepancy, which becomes significant for lower redshifts and can produce few % errors in the power spectrum amplitude.

These results indicate that the existing PT-based approaches fail to describe the two competitive effects of redshift distortion in the power spectrum.[1] A proper account of these is thus essential in accurately modeling BAOs.

B. Phenomenological model description

Next consider the phenomenological models of redshift distortion, which have been originally introduced to explain the observed power spectrum on small scales. Although the relation between the model and exact expression (4) is less clear, for most of the models frequently used in the literature, the redshift-space power spectrum is expressed in the form (e.g., [42,49–54])

$$P^{(S)}(k,\mu) = D_{\mathrm{FoG}}[k\mu f\sigma_v]P_{\mathrm{Kaiser}}(k,\mu), \tag{9}$$

where the term $P_{\mathrm{Kaiser}}(k,\mu)$ represents the Kaiser effect, and the term $D_{\mathrm{FoG}}[k\mu f\sigma_v]$ indicates a damping function which mimics the Finger-of-God effect. The quantity σ_v is the one-dimensional velocity dispersion defined by $\sigma_v^2 = \langle u_z^2(0)\rangle$. The variety of the functional forms for $P_{\mathrm{Kaiser}}(k,\mu)$ and $D_{\mathrm{FoG}}[k\mu f\sigma_v]$ is summarized as follows.

The Kaiser effect has been first recognized from the linear-order calculations [43], from which the enhancement factor $(1+f\mu^2)^2$ is obtained [see Eq. (5)]. As a simple description for the Kaiser effect, one may naively multiply the nonlinear matter power spectrum by this factor, just by hand. Recently, proper account of the nonlinear effect has been discussed [42,49], and a nonlinear model of the Kaiser effect has been proposed using the real-space power spectra. Thus, we have

$$P_{\mathrm{Kaiser}}(k,\mu) = \begin{cases} (1+f\mu^2)^2 P_{\delta\delta}(k) & \text{linear,} \\ P_{\delta\delta}(k) + 2f\mu^2 P_{\delta\theta}(k) + f^2\mu^4 P_{\theta\theta}(k) & \text{nonlinear.} \end{cases} \tag{10}$$

[1]Nevertheless, it should be noted that the Lagrangian PT would still be powerful in predicting the two-point correlation function around the baryon acoustic peak. In both real and redshift spaces, the prediction reasonably recovers the smeared peak and trough structures, and it gives a better agreement with N-body simulation.

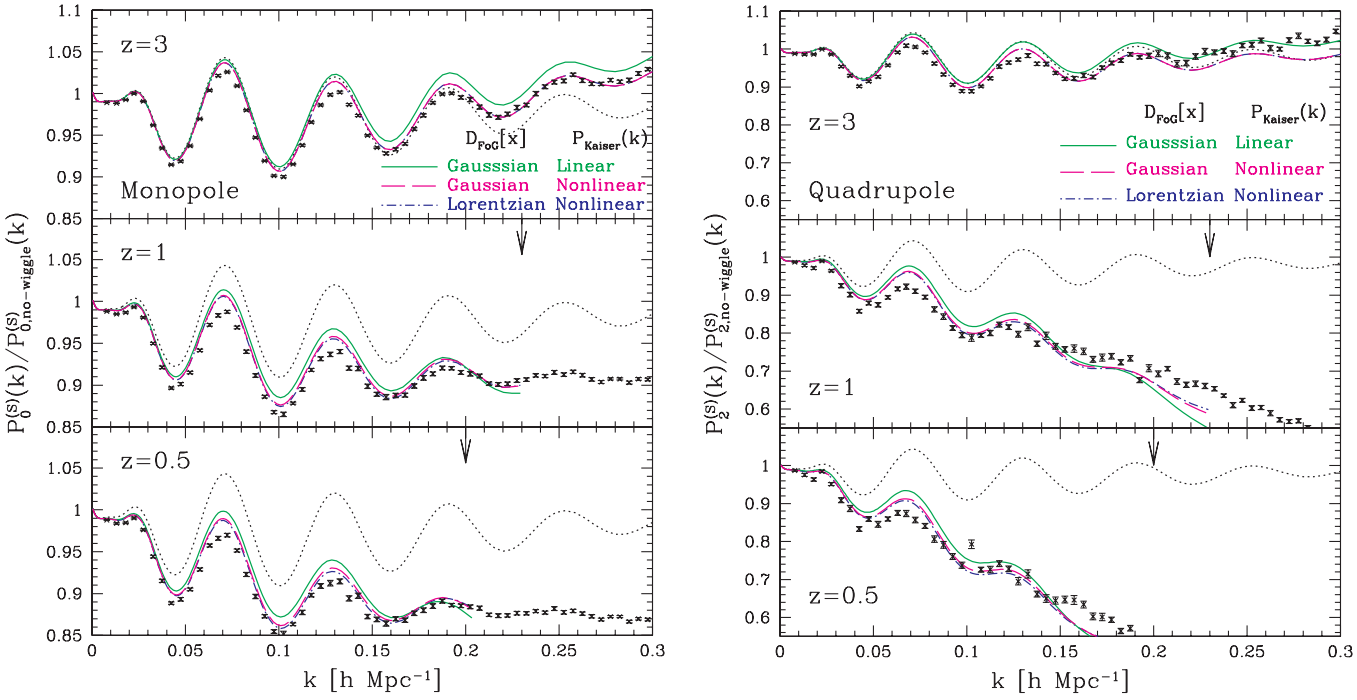

FIG. 2 (color online). Same as in Fig. 1, but here we plot the results of phenomenological model predictions. The three different predictions depicted as solid, dashed, dot-dashed lines are based on the phenomenological model of redshift distortion (9) with various choices of Kaiser and Finger-of-God terms [Eqs. (10) and (11)]. The left panel shows the monopole power spectra ($\ell = 0$), and the right panel shows the quadrupole spectra ($\ell = 2$). In all cases, the one-dimensional velocity dispersion σ_v was determined by fitting the predictions to the N-body simulations. In each panel, the vertical arrows indicate the maximum wave number $k_{1\%}$ for improved PT prediction including up to the second-order Born approximation [see Eq. (12) for a definition].

Here, the spectra $P_{\delta\delta}$, $P_{\theta\theta}$, and $P_{\delta\theta}$ denote the auto power spectra of density and velocity divergence, and their cross power spectrum, respectively. The velocity divergence θ is defined by $\theta \equiv \nabla \boldsymbol{u} = -\nabla \boldsymbol{v}/(aHf)$.[2]

On the other hand, the functional form of the damping term can be basically modeled from the distribution function of one-dimensional velocity. Historically, it is characterized by a Gaussian or exponential function (e.g., [51–54]), which leads to

$$D_{\rm FoG}[x] = \begin{cases} \exp(-x^2) & \text{Gaussian,} \\ 1/(1+x^2) & \text{Lorentzian.} \end{cases} \tag{11}$$

Note that there is an analogous expression for the exponential distribution, i.e., $D_{\rm FoG}[x] = 1/(1+x^2/2)^2$ [50], but the resultant power spectrum is quite similar to the one adopting the Lorentzian form for the range of our interest, $x \lesssim 1$. Since the Finger-of-God effect is thought to be a fully nonlinear effect, which mostly comes from the virialized random motion of the mass (or galaxy) residing in a halo, the prediction of σ_v seems rather difficult. Our primary purpose is to model the shape and structure of the acoustic feature in the power spectrum, and the precise form of the damping is basically irrelevant. We thus regard σ_v as a free parameter and determine it by fitting the predictions to the simulations or observations.

Figure 2 compares the phenomenological models of redshift distortion with combination of Eqs. (10) and (11) with N-body simulations. In computing the redshift-space power spectrum from the phenomenological models, we adopt the improved PT treatment by Refs. [33,34], and the analytic results including the corrections up to the second-order Born approximation are used to obtain the three different power spectra $P_{\delta\delta}$, $P_{\delta\theta}$, and $P_{\theta\theta}$. The accuracy of the improved PT treatment has been checked in detail by Ref. [34], and it has been shown that the predictions of $P_{\delta\delta}$ reproduce the N-body results quite well within 1% accuracy below the wave number $k_{1\%}$, indicated by the vertical arrows in Fig. 2. This has been calibrated from a proper comparison between N-body and PT results and is empirically characterized by solving the following equation [25,34]:

$$\frac{k_{1\%}^2}{6\pi^2}\int_0^{k_{1\%}} dq P_{\rm lin}(q;z) = C \tag{12}$$

with $C = 0.7$ and $P_{\rm lin}$ being the linear matter spectrum. Note that the 1% accuracy of the improved PT prediction at

[2]The sign convention of the definition of velocity divergence θ differs from that of Refs. [33,34], but is equivalent to the one in Refs. [26–28,42].

$z = 3$ is reached at $k \sim 0.47h$ Mpc^{-1}, outside the plot range. We basically use this criterion to determine σ_v, and fit the predictions of both the monopole and quadrupole spectra to the N-body results in the range $0 \le k \le k_{1\%}$.

Since we allow σ_v to vary as a free parameter, the overall behavior of the model predictions reproduces the N-body results, and the differences between model predictions are basically small compared to the results in the PT description. However, there still exist small but non-negligible discrepancies between N-body results and model predictions, which are statistically significant, and are comparable to or exceed the expected errors in upcoming BAO measurements [34]. Although the agreement is somehow improved when we adopt the nonlinear model of $P_{\rm Kaiser}$, there still remain discrepancies of a few % in monopole and 5% in quadrupole moments of the power spectrum amplitudes. These are irrespective of the choice of damping function $D_{\rm FoG}$.

Furthermore, the fitted results of σ_v show a somewhat peculiar behavior. Figure 3 plots the fitted values of σ_v as a function of redshift (symbols), which significantly deviate from the linear-theory prediction (solid line) at increasing redshifts. At $z = 3$, the fitted result eventually approaches zero in order to minimize the residuals in fitting the prediction to simulations. This could happen when we account for a slight damping at low k and a small enhancement at high k in power spectrum amplitudes. The fitted results of σ_v are in contrast with naive expectations and indicate that the model based on the expression (9) misses something important and needs to be reconsidered.

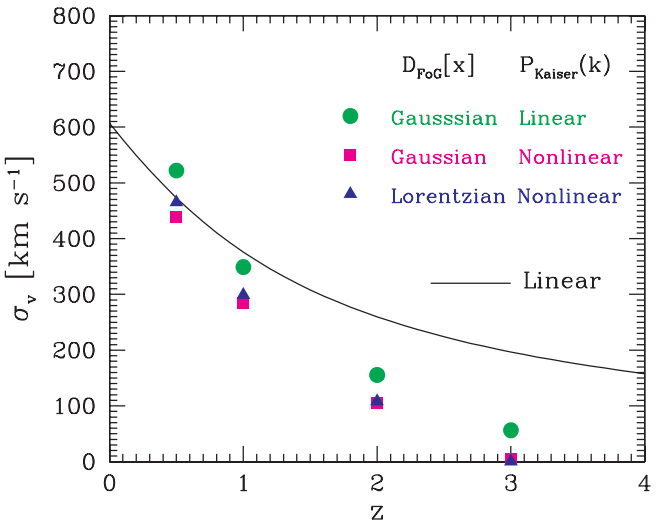

FIG. 3 (color online). Redshift evolution of velocity dispersion σ_v determined by fitting the predictions of monopole and quadrupole power spectra to the N-body results. The solid line represents the linear-theory prediction, while the symbols indicate the results obtained by fitting the models of redshift distortion with various choices of Kaiser and damping terms (see Fig. 2).

IV. IMPROVED MODEL PREDICTION

A. Derivation

The comparison in the previous section reveals that even in the models with a fitting parameter, a small but non-negligible discrepancy appears at the scales of BAOs, where the choice of the damping function $D_{\rm FoG}[x]$ does not sensitively affect the predictions. This implies that there exist missing terms arising from the nonlinear mode coupling between density and velocity fields, and those corrections alter the acoustic feature in the redshift-space power spectrum. In this section, starting with the exact expression (4), we derive nonlinear corrections, which are relevant to explain the modulation of acoustic features in redshift space.

First recall that the expression (4) is written in the form

$$P^{(S)}(k, \mu) = \int d^3\boldsymbol{x} e^{i\boldsymbol{k}\cdot\boldsymbol{x}} \langle e^{j_1 A_1} A_2 A_3 \rangle, \tag{13}$$

where the quantities j_1, A_i $(i = 1, 2, 3)$ are, respectively, given by

$$j_1 = -ik\mu f, \qquad A_1 = u_z(\boldsymbol{r}) - u_z(\boldsymbol{r}'),$$
$$A_2 = \delta(\boldsymbol{r}) + f\nabla_z u_z(\boldsymbol{r}), \qquad A_3 = \delta(\boldsymbol{r}') + f\nabla_z u_z(\boldsymbol{r}').$$

We shall rewrite the ensemble average $\langle e^{j_1 A_1} A_2 A_3 \rangle$ in terms of cumulants. To do this, we use the relation between the cumulant and moment generating functions. For the stochastic vector field $\boldsymbol{A} = \{A_1, A_2, A_3\}$, we have (e.g., [29,42])

$$\langle e^{\boldsymbol{j}\cdot\boldsymbol{A}} \rangle = \exp\{\langle e^{\boldsymbol{j}\cdot\boldsymbol{A}} \rangle_c\} \tag{14}$$

with $\boldsymbol{j}$ being an arbitrary constant vector, $\boldsymbol{j} = \{j_1, j_2, j_3\}$. Taking the derivative twice with respect to j_2 and j_3, we then set $j_2 = j_3 = 0$. We obtain [42]

$$\langle e^{j_1 A_1} A_2 A_3 \rangle = \exp\{\langle e^{j_1 A_1} \rangle_c\}[\langle e^{j_1 A_1} A_2 A_3 \rangle_c + \langle e^{j_1 A_1} A_2 \rangle_c \langle e^{j_1 A_1} A_3 \rangle_c]. \tag{15}$$

Substituting this into Eq. (13), we arrive at

$$P^{(S)}(k, \mu) = \int d^3\boldsymbol{x} e^{i\boldsymbol{k}\cdot\boldsymbol{x}} \exp\{\langle e^{j_1 A_1} \rangle_c\}[\langle e^{j_1 A_1} A_2 A_3 \rangle_c + \langle e^{j_1 A_1} A_2 \rangle_c \langle e^{j_1 A_1} A_3 \rangle_c]. \tag{16}$$

This expression clearly reveals the coupling between density and velocity fields associated with the Kaiser and Finger-of-God effects. In addition to the prefactor $\exp\{\langle e^{j_1 A_1} \rangle_c\}$, the ensemble averages over the quantities A_2 and A_3 responsible for the Kaiser effect all include the exponential factor $e^{j_1 A_1}$, which can produce a non-negligible correlation between density and velocity.

Comparing Eq. (16) with the expression (9) with (10) and (11), we deduce that the phenomenological models discussed in Sec. III B miss something important and are derived based on several assumptions or treatments:

(i) In the integrand of Eq. (16), while taking the limit $j_1 \to 0$ in the bracket, we keep $j_1 \neq 0$ in the exponent of the prefactor.
(ii) For cumulants $\langle A_1^n \rangle_c = \langle [u_z(\boldsymbol{r}) - u_z(\boldsymbol{r}')]^n \rangle_c$ of any integer value n, the spatial correlations between different positions are ignored, and the nonvanishing cumulants are assumed to be expressed as $\langle A_1^n \rangle_c \simeq 2\langle u_z^n \rangle_c = 2c_n \sigma_{\rm v}^n$ for even n, with c_n being constants.
(iii) To further obtain the Gaussian or Lorentzian forms of the damping function $D_{\rm FoG}[x]$, we assume that the conditions, $c_n = 0$ except for $c_2 = 1$, or, $c_{2n} = (2n-1)!$ and $c_{2n-1} = 0$, are fulfilled.

In the above, the last two conditions play a role for specifying the damping function, and they mainly affect the broadband shape of the power spectrum. On the other hand, the first condition leads to the expression of $P_{\rm Kaiser}(k)$, which can add the most dominant contribution to the acoustic feature in the power spectrum. Since the choice of the damping function (11) is presumably a minor source for discrepancies between the model predictions and simulations, taking the limit $j_1 \to 0$ in the bracket would be the main reason for discrepancy. In this respect, the terms involving the exponential factor can produce additional contributions to the spectrum $P_{\rm Kaiser}(k)$, which are responsible for explaining the modulated acoustic peak and trough structure in redshift space.

Let us now derive the corrections to $P_{\rm Kaiser}(k)$. To do this, we keep the last two conditions, and perturbatively treat the terms inside the bracket of Eq. (16). This treatment is reasonable, because the modification of acoustic features should be small for relevant scales of BAOs. On the other hand, the factor $\exp\{\langle e^{j_1 A_1} \rangle_c\}$ is most likely affected by the virialized random motion of the mass around halos, and seems difficult to treat perturbatively. Here, regarding the quantity j_1 as a small expansion parameter, we perturbatively expand the terms in the bracket of the integrand. Up to the second order in j_1, we have

$$\begin{aligned}&\langle e^{j_1 A_1} A_2 A_3 \rangle_c + \langle e^{j_1 A_1} A_2 \rangle_c \langle e^{j_1 A_1} A_3 \rangle_c \\ &\simeq \langle A_2 A_3 \rangle + j_1 \langle A_1 A_2 A_3 \rangle_c \\ &\quad + j_1^2 \{\tfrac{1}{2}\langle A_1^2 A_2 A_3 \rangle_c + \langle A_1 A_2 \rangle_c \langle A_1 A_3 \rangle_c\} + \mathcal{O}(j_1^3). \quad (17)\end{aligned}$$

In the above, the term $\langle A_1^2 A_2 A_3 \rangle_c$ turns out to be higher order when we explicitly compute it employing the perturbation theory calculation, and is roughly proportional to $\mathcal{O}(P_{\rm lin}^3)$. We thus drop the higher-order contribution, and collect the leading and next-to-leading order contributions. Then, Eq. (16) can be recast as

$$\begin{aligned}P^{(\rm S)}(k,\mu) = D_{\rm FoG}[k\mu f\sigma_{\rm v}]\{&P_{\delta\delta}(k) + 2f\mu^2 P_{\delta\theta}(k) \\ &+ f^2\mu^4 P_{\theta\theta}(k) + A(k,\mu) + B(k,\mu)\}. \quad (18)\end{aligned}$$

Here, we replaced the exponential prefactor $\exp\{\langle e^{j_1 A_1} \rangle_c\}$ with the damping function $D_{\rm FoG}$. The corrections A and B are, respectively, given by

$$\begin{aligned}A(k,\mu) &= j_1 \int d^3\boldsymbol{x} e^{i\boldsymbol{k}\cdot\boldsymbol{x}} \langle A_1 A_2 A_3 \rangle_c, \\ B(k,\mu) &= j_1^2 \int d^3\boldsymbol{x} e^{i\boldsymbol{k}\cdot\boldsymbol{x}} \langle A_1 A_2 \rangle_c \langle A_1 A_3 \rangle_c.\end{aligned}$$

In terms of the basic quantities of density δ and velocity divergence $\theta = -\nabla\boldsymbol{v}/(aHf)$, they are rewritten as

$$\begin{aligned}A(k,\mu) = (k\mu f) \int \frac{d^3\boldsymbol{p}}{(2\pi)^3} \frac{p_z}{p^2} \{&B_\sigma(\boldsymbol{p}, \boldsymbol{k}-\boldsymbol{p}, -\boldsymbol{k}) \\ &- B_\sigma(\boldsymbol{p}, \boldsymbol{k}, -\boldsymbol{k}-\boldsymbol{p})\}, \quad (19)\end{aligned}$$

$$B(k,\mu) = (k\mu f)^2 \int \frac{d^3\boldsymbol{p}}{(2\pi)^3} F(\boldsymbol{p}) F(\boldsymbol{k}-\boldsymbol{p}); \quad (20)$$

$$F(\boldsymbol{p}) = \frac{p_z}{p^2}\left\{P_{\delta\theta}(p) + f\frac{p_z^2}{p^2} P_{\theta\theta}(p)\right\},$$

where the function B_σ is the cross bispectra defined by

$$\begin{aligned}&\left\langle \theta(\boldsymbol{k}_1)\left\{\delta(\boldsymbol{k}_2) + f\frac{k_{2z}^2}{k_2^2}\theta(\boldsymbol{k}_2)\right\}\left\{\delta(\boldsymbol{k}_3) + f\frac{k_{3z}^2}{k_3^2}\theta(\boldsymbol{k}_3)\right\}\right\rangle \\ &\quad = (2\pi)^3 \delta_D(\boldsymbol{k}_1 + \boldsymbol{k}_2 + \boldsymbol{k}_3) B_\sigma(\boldsymbol{k}_1, \boldsymbol{k}_2, \boldsymbol{k}_3). \quad (21)\end{aligned}$$

In deriving the expression (18), while we employed the low-k expansion, we do not assume that the terms A_i themselves are entirely small. In this sense, the expressions (18)–(20) still have some nonperturbative properties, although the new corrections A and B neglected in the previous phenomenological models are expected to be small, and can be treated perturbatively. In Appendix A, based on the standard PT treatment, we summarize the perturbative expressions for the corrections (19) and (20), in which the three-dimensional integrals are reduced to the sum of one- and two-dimensional integrals.

To see the significance of the newly derived terms A and B, we evaluate the monopole and quadrupole contributions to the functions defined by

$$P_{\ell,\rm corr}^{(\rm S)}(k) \equiv \frac{2\ell+1}{2} \int_{-1}^{1} d\mu D_{\rm FoG}(k\mu f\sigma_{\rm v}) \{\begin{matrix} A(k,\mu) \\ B(k,\mu) \end{matrix}\}. \quad (22)$$

The results are then plotted in Fig. 4, divided by the smoothed reference spectrum, $P_{\ell,\text{no-wiggle}}^{(\rm S)}(k)$. In plotting the results, we specifically assume the Gaussian form of $D_{\rm FoG}$, and adopt the linear theory to estimate $\sigma_{\rm v}$ [see Eq. (7)].

The corrections coming from the A term show oscillatory behavior and tend to have a larger amplitude than those from the B term. While the corrections from the B term are basically smooth and small, they still yield a non-negligible contribution, especially for the quadrupole power spectrum. Although the actual contributions of these

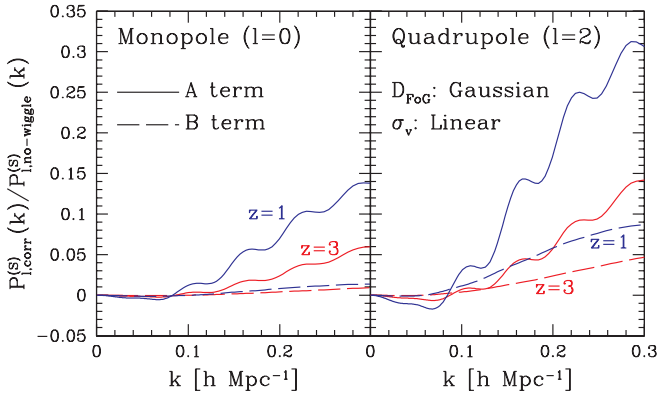

FIG. 4 (color online). Contributions of power spectrum corrections coming from the A and B terms divided by the smooth reference power spectrum, $P^{(S)}_{\ell,\mathrm{corr}}(k)/P^{(S)}_{\ell,\text{no-wiggle}}(k)$ [Eq. (22)]. We adopt the Gaussian form of the damping function D_{FoG} with σ_v computed from linear theory [see Eq. (7)]. Left and right panels, respectively, show the monopole and quadrupole power spectra at redshifts $z = 3$ and 1.

corrections to the total power spectrum are determined by the fitting parameter σ_v, and thus the resultant amplitudes shown in Fig. 4 do not simply reflect the correct amplitudes, the new corrections A and B can definitely give an important contribution to the acoustic feature in the power spectrum.

Finally, it is interesting to note that while the new formula for redshift-space power spectrum (18) would be applicable to the nonlinear regime where the standard PT calculation breaks down, the resultant expression itself is similar to the one for the redshift-space power spectrum in one-loop standard PT. The one-loop power spectrum in redshift space, $P^{(S)}_{\mathrm{SPT}}(k,\mu)$ given at Eq. (5), can be formally recast as

$$P^{(S)}_{\mathrm{SPT}}(k,\mu) = \{1-(k\mu f\sigma_{v,\mathrm{lin}})^2\}\{P_{\delta\delta}(k) + 2f\mu^2 P_{\delta\theta}(k) + f^2\mu^4 P_{\theta\theta}(k)\} + A(k,\mu) + B(k,\mu) + C(k,\mu). \quad (23)$$

Note that each term in the above expression should be consistently evaluated using the perturbative solutions up to the third order in δ and θ, and as a result, only the leading-order corrections proportional to $P_{\mathrm{lin}}\Delta^2$ (or equivalently the fourth order in $\delta^{(1)}$) are included in the one-loop power spectrum. Here, the function C is defined by

$$\begin{aligned} C(k,\mu) &= (k\mu f)^2 \int \frac{d^3\boldsymbol{p}d^3\boldsymbol{q}}{(2\pi)^3}\delta_{\mathrm{D}}(\boldsymbol{k}-\boldsymbol{p}-\boldsymbol{q})\frac{\mu_p^2}{p^2}P_{\theta\theta}(p) \\ &\quad\times\{P_{\delta\delta}(q) + 2f\mu_q^2 P_{\delta\theta}(q) + f^2\mu_q^4 P_{\theta\theta}(q)\} \\ &\simeq (k\mu f)^2 \int \frac{d^3\boldsymbol{p}d^3\boldsymbol{q}}{(2\pi)^3}\delta_{\mathrm{D}}(\boldsymbol{k}-\boldsymbol{p}-\boldsymbol{q})\frac{\mu_p^2}{p^2} \\ &\quad\times(1+f\mu_q^2)^2 P_{\mathrm{lin}}(p)P_{\mathrm{lin}}(q) \end{aligned} \quad (24)$$

with $\mu_p = p_z/|\boldsymbol{p}|$ and $\mu_q = q_z/|\boldsymbol{q}|$. The second equality is valid for the one-loop PT calculation. Hence, if we adopt either the Lorentzian or Gaussian form in Eq. (11) and just expand it in powers of its argument, the new formula (18) reduces to the one-loop result (23) by just dropping the term C.

The C term originates from the spatial correlation of the velocity field and is obtained through the low-k expansion of the exponential prefactor $\exp\{\langle e^{j_1 A_1}\rangle_c\}$ in Eq. (16). For the scales of BAOs, the C term monotonically increases the amplitude of the power spectrum, and it does not alter the acoustic structure drastically. Indeed, our several examinations reveal that the effect of this can be effectively absorbed into the damping function $D[k\mu f\sigma_v]$ by varying the velocity dispersion σ_v. Rather, the main drawback of the standard PT expression (23) comes from a naive expansion of all the terms in the exact formula (4), which fails to describe the delicate balance between the Finger-of-God damping and the enhancement from the Kaiser effect and nonlinear gravitational growth. As we will see in the next section, both keeping the damping term D_{FoG} and including the corrections A and B seem essential, and with this treatment, even the standard PT calculation of the power spectrum can give an excellent result which reproduces the N-body simulations fairly well.

B. Comparison with N-body simulations

We now compare the new prediction for the redshift-space power spectra with the result of N-body simulations. Figure 5 shows the monopole (left panel) and quadrupole (right panel) power spectra divided by their smooth reference spectra. The analytical predictions based on the model (18) are plotted adopting the Gaussian form of the Finger-of-God term $D_{\mathrm{FoG}}[kf\mu\sigma_v]$, and the velocity dispersion σ_v is determined by fitting the predictions to the N-body results. In computing the predictions, the A and B terms are calculated from the one-loop standard PT results in Appendix A, while the spectra $P_{\delta\delta}$, $P_{\delta\theta}$, and $P_{\theta\theta}$ are obtained from improved PT in solid lines, and from standard PT in dashed lines.

Compared to Figs. 1 and 2, the agreement between N-body simulations and predictions depicted as solid lines is clearly improved, and the prediction including the corrections faithfully traces the N-body trends of the acoustic feature, especially around $k = 0.05 \sim 0.15h$ Mpc^{-1}, where the phenomenological model shows a few % level discrepancy. A remarkable point is that a reasonable agreement basically holds over the range below the critical wave number $k_{1\%}$ calibrated in real space [vertical arrows, Eq. (12) for definition]. This is also true for the case adopting one-loop standard PT to compute $P_{\delta\delta}$, $P_{\delta\theta}$, and $P_{\theta\theta}$ (dashed lines), and the range of agreement is wider than that of the existing PT-based models in Sec. III A.

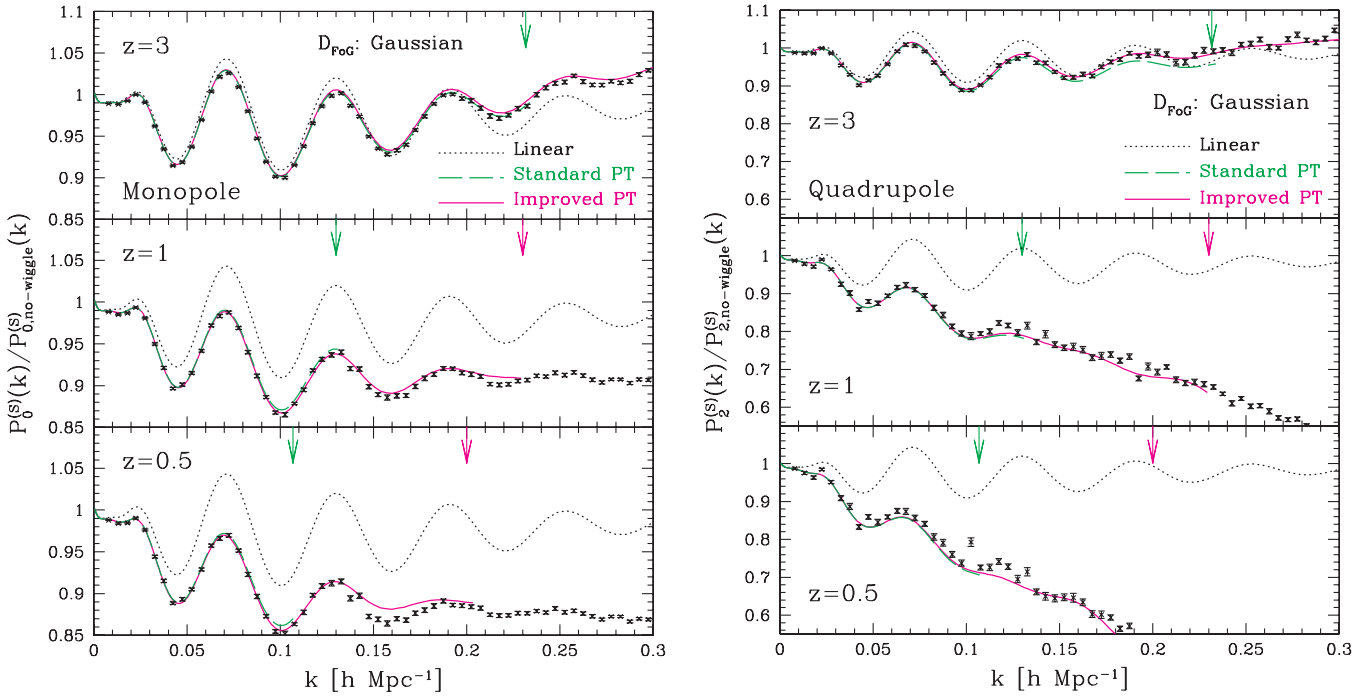

FIG. 5 (color online). Same as in Fig. 2, but here we adopt a new model of redshift distortion (18). Solid and dashed lines represent the predictions for which the spectra $P_{\delta\delta}$, $P_{\delta\theta}$, and $P_{\theta\theta}$ are obtained from the improved PT including the correction up to the second-order Born correction, and one-loop calculations of the standard PT, respectively. In both cases, the corrections A and B given in Eqs. (19) and (20) are calculated from standard PT results (see Appendix A). The vertical arrows indicate the maximum wave number $k_{1\%}$ defined in Eq. (12), for standard PT and improved PT (from left to right).

In Fig. 6, to see the significance of the contributions from corrections A and B, we divide the improved PT prediction for the power spectra $P^{(S)}(k)$ at $z = 1$ into the three pieces as $P^{(S)}_{\rm Kaiser}$, $P^{(S)}_{{\rm corr},A}$, and $P^{(S)}_{{\rm corr},B}$, which are separately plotted as dotted, long-dashed, and short dashed lines, respectively. The power spectrum $P^{(S)}_{\rm Kaiser}$ is the contribution of the nonlinear Kaiser term given in Eq. (10), convolved with the damping function $D_{\rm FoG}$. The spectra $P^{(S)}_{{\rm corr},A}$ and $P^{(S)}_{{\rm corr},B}$ represent the actual contributions of the corrections A and B defined by Eq. (22), with a fitted value of σ_v. The corrections A and B give different contributions in the amplitude of the monopole and quadrupole spectra, and their total contribution can reach $\sim$10% and $\sim$40% for monopole and quadrupole spectra at $k \lesssim 0.2h$ Mpc^{-1}, respectively. Thus, even though the resultant shape of the total spectrum $P^{(S)}(k)$ apparently resembles the one obtained from the phenomenological model, the actual contribution of the corrections A and B would be large and cannot be neglected.

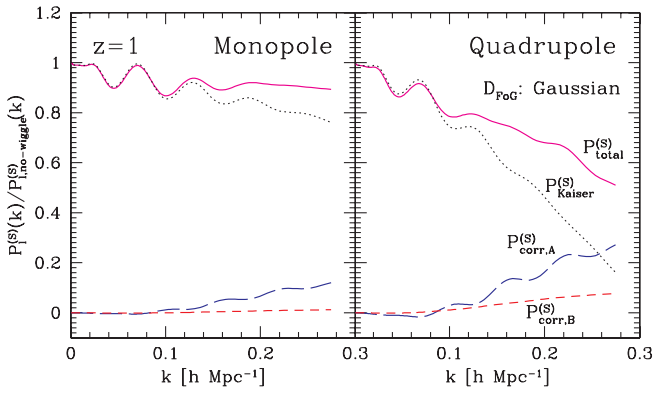

FIG. 6 (color online). Contribution of each term in the redshift-space power spectrum. For monopole ($\ell = 0$, left) and quadrupole ($\ell = 2$, right) spectra of the improved model prediction at $z = 1$ shown as solid lines of Fig. 5, we divide the total power spectrum $P^{(S)}_{\rm total}$ (solid) into the three pieces as $P^{(S)}_{\rm total} = P^{(S)}_{\rm Kaiser} + P^{(S)}_{{\rm corr},A} + P^{(S)}_{{\rm corr},B}$, and each contribution is separately plotted dividing by smoothed reference spectra, $P^{(S)}_{\ell,{\rm no\text{-}wiggle}}$. Here, the spectrum $P^{(S)}_{\rm Kaiser}$ (dotted) is the contribution of the nonlinear Kaiser term (10) convolved with the Finger-of-God damping $D_{\rm FoG}$, and the corrections $P^{(S)}_{{\rm corr},A}$ and $P^{(S)}_{{\rm corr},B}$ are those given by Eq. (22).

Note, however, that a closer look at low-z behavior reveals a slight discrepancy around $k \sim 0.15h$ Mpc^{-1} and $0.22h$ Mpc^{-1} in the monopole spectrum. Also, discrepancies in the quadrupole spectrum seem a bit large, and eventually reach $\sim$5% error in some wave numbers at $z = 0.5$. This is partially ascribed to our heterogeneous treatment on the corrections A and B using the standard PT calculations. It is known that the standard PT result generically gives rise to a strong damping in the BAOs, and it incorrectly leads to a phase reversal of the BAOs. Thus, beyond the validity regime of the standard PT, the predic-

tions including the small corrections tend to oversmear the acoustic feature, leading to a small discrepancy shown in Fig. 5.

Another source for the discrepancies may come from the effect of finite-mode sampling caused by the finite box size of the N-body simulations. As advocated by Refs. [25,55], due to the finite number of Fourier modes, the matter power spectrum measured from N-body simulations may not agree well with the predictions of linear theory nor standard PT even at very large scales, and tends to systematically deviate from them. While we follow and extend the procedure of Ref. [25] to correct this effect in redshift space, it relies on the leading-order calculations of standard PT, and the correction for finite-mode sampling has been restricted to the low-k modes, $k \lesssim 0.1h\ \mathrm{Mpc}^{-1}$ [34]. Hence, the high-k modes of the power spectrum plotted here may be affected by the effect of finite-mode sampling, and it would be significant for higher-multipole spectra because of its small amplitude. This might still be serious even with the 30 independent N-body simulations.

Perhaps, the best way to remedy these discrepancies at low-z is both to apply the improved PT treatment to the corrections A and B, and to consider the higher-order contributions for correcting the effect of finite-mode sampling over the relevant range of BAOs. The complete analysis along this line needs some progress and is beyond the scope of this paper. Nevertheless, it should be stressed that the model given by Eq. (18) captures several important aspects of redshift distortion, and even the present treatment with standard PT calculations of the corrections A and B can provide a better description for power spectra. In Fig. 7, we plot the fitted values of the velocity dispersion obtained from the new predictions shown in Fig. 5. The redshift dependence of the fitted results roughly matches physical intuition, and is rather consistent with the linear-theory prediction. This is contrasted to the cases neglecting the corrections (see Fig. 3).

As another significance, we plot in Fig. 8 the quadrupole-to-monopole ratios for redshift-space power spectra. The new model predictions using standard and improved PT calculations (solid and dashed lines) are compared with those neglecting the corrections A and B (dot-dashed lines). The amplitude of the ratio $P_2^{(S)}/P_0^{(S)}$ basically reflects the strength of the clustering anisotropies, and is proportional to $(4f/3 + 4f^2/7)/(1 + 2f/3 + f^2/5)$ in the limit $k \to 0$ (e.g., [1,3,43]). One noticeable point is that the N-body results for the quadrupole-to-monopole ratio do exhibit oscillatory behavior, and the model including the corrections (18) reproduces the N-body trends fairly well. On the other hand, the phenomenological model neglecting the corrections generally predicts the smooth scale dependence of the ratio $P_2^{(S)}/P_0^{(S)}$, and thus it fails to reproduce the oscillatory feature. Since this oscillation originates from the acoustic feature in BAOs,

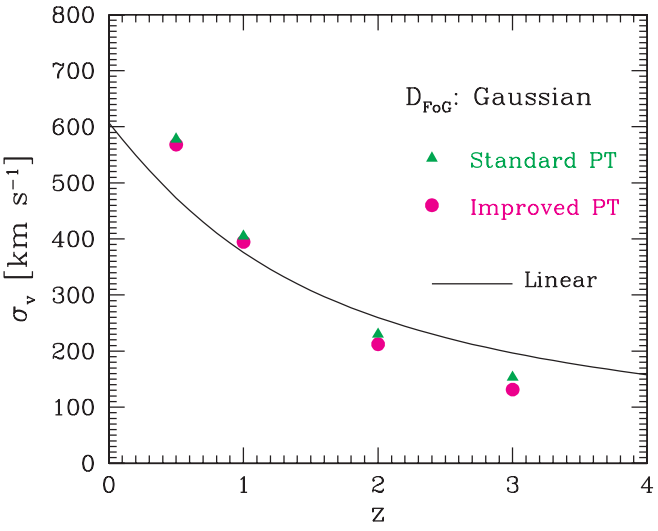

FIG. 7 (color online). Same as in Fig. 3, but here we adopt the new model of redshift distortion in estimating σ_v. The filled triangles and circles are the results obtained from predictions based on standard PT and improved PT calculations, respectively (see dashed and solid lines in Fig. 5).

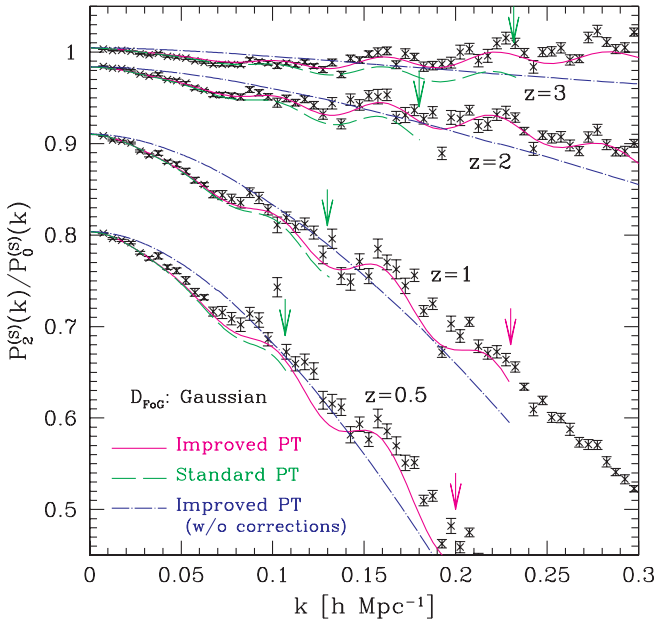

FIG. 8 (color online). Quadrupole-to-monopole ratios for the redshift-space power spectrum, $P_2^{(S)}(k)/P_0^{(S)}(k)$, given at $z = 3$, 2, 1, and 0.5 (from top to bottom). Solid and dashed lines, respectively, represent the predictions based on the new model of redshift distortion combining improved PT and standard PT calculation to estimate the three different power spectra $P_{\delta\delta}$, $P_{\delta\theta}$, and $P_{\theta\theta}$. Dot-dashed lines are the results based on the phenomenological model neglecting the corrections, which correspond to solid lines in Fig. 2 (i.e., nonlinear P_{Kaiser} + Gaussian, D_{FoG}). The vertical arrows indicate the maximum wave number $k_{1\%}$ for standard PT (left, green) and improved PT (right, magenta).

Fig. 8 implies that the quadrupole-to-monopole ratio possesses helpful information not only to constrain the growth-rate parameter f, but also to determine the acoustic scales. In other words, any theoretical template for the redshift-space power spectrum neglecting the corrections A and B may produce a systematic bias in determining the growth-rate parameter $f(z)$, Hubble parameter $H(z)$, and angular diameter distance $D_A(z)$, which we will discuss in detail in the next section.

V. IMPLICATIONS

The primary science goal of future galaxy surveys is to clarify the nature of late-time cosmic acceleration, and thereby constraining the parameters $D_A(z)$, $H(z)$, and $f(z)$ through a precise measurement of BAOs in redshift space would be the most important task. However, these constraints may be biased if we use the incorrect model of redshift distortion as a theoretical template fitting to observations. In this section, we explore the potential impact on the uncertainty and bias in the parameter estimation for $D_A(z)$, $H(z)$, and $f(z)$.

A. Recovery of parameters D_A, H, and f

Let us first examine the parameter estimation using the new model of redshift distortion. Fitting the theoretical template for the power spectrum to the N-body data, we will check if the best-fit parameters for $D_A(z)$, $H(z)$, and $f(z)$ can be correctly recovered from the monopole and quadrupole moments of anisotropic BAOs.

We model the power spectrum of N-body simulations by

$$P^{(\mathrm{S})}_{\mathrm{model}}(k,\mu) = \frac{H(z)}{H_{\mathrm{fid}}(z)}\left\{\frac{D_{A,\mathrm{fid}}(z)}{D_A(z)}\right\}^2 P^{(\mathrm{S})}(q,\nu), \tag{25}$$

where the comoving wave number k and the directional cosine μ for the underlying cosmological model are related to the true ones q and ν by the Alcock-Paczynski effect through (e.g., [18,53,54])

$$q = k\left[\left(\frac{D_{A,\mathrm{fid}}}{D_A}\right)^2 + \left\{\left(\frac{H}{H_{\mathrm{fid}}}\right) - \left(\frac{D_{A,\mathrm{fid}}}{D_A}\right)^2\right\}\mu^2\right]^{1/2}, \tag{26}$$

$$\nu = \left(\frac{H}{H_{\mathrm{fid}}}\right)\mu\left[\left(\frac{D_{A,\mathrm{fid}}}{D_A}\right)^2 + \left\{\left(\frac{H}{H_{\mathrm{fid}}}\right) - \left(\frac{D_{A,\mathrm{fid}}}{D_A}\right)^2\right\}\mu^2\right]^{-1/2}. \tag{27}$$

The quantities $D_{A,\mathrm{fid}}$ and H_{fid} are the fiducial values of the angular diameter distance and Hubble parameter adopted in the N-body simulations. For a given set of cosmological parameters, the redshift-space power spectrum $P^{(\mathrm{S})}$ is calculated from Eq. (18), but we here treat the quantity f as a free parameter in addition to the velocity dispersion σ_{v}. Further, to mimic a practical data analysis using galaxy power spectrum, we introduce the bias parameter b, assuming a linear deterministic relation, i.e., $\delta_{\mathrm{sim}} = b\delta_{\mathrm{m}}$.[3] Then, fitting the monopole and quadrupole power spectra of Eq. (25) to those of the N-body simulation at $z = 1$, we determine the best-fit values of D_A, H, and f, just marginalized over the parameters σ_{v} and b. To do this, we use the Markov chain Monte Carlo (MCMC) technique described by Ref. [56], and adopt the likelihood function given by

$$-2\ln\mathcal{L} = \sum_n \sum_{\ell,\ell'=0,2} \{P^{(\mathrm{S})}_{\ell,\mathrm{sim}}(k_n) - P^{(\mathrm{S})}_{\ell,\mathrm{model}}(k_n)\}\mathrm{Cov}^{-1}_{\ell,\ell'}(k_n) \times \{P^{(\mathrm{S})}_{\ell',\mathrm{sim}}(k_n) - P^{(\mathrm{S})}_{\ell',\mathrm{model}}(k_n)\}, \tag{28}$$

where the quantity $\mathrm{Cov}_{\ell,\ell'}$ represents the covariance matrix between different multipoles. The range of wave number used in the likelihood analysis was chosen as $k \le k_{\mathrm{max}} = 0.205h\ \mathrm{Mpc}^{-1}$, so as to satisfy $k_{\mathrm{max}} \le k_{1\%}$. As for the covariance, we simply ignore the non-Gaussian contribution (see Ref. [57] for validity of this treatment), and use the linear theory to estimate the diagonal components of the covariance, $\mathrm{Cov}_{\ell,\ell'}$, including the effect of shot-noise contribution assuming the galaxy number density $\bar{n}_{\mathrm{g}} = 5\times10^{-4}h^3\ \mathrm{Mpc}^{-3}$. The explicit expression for the covariance is presented in Appendix C. We checked that the linear-theory estimate reasonably reproduces the N-body results of the covariance matrix for the range of our interest $k \lesssim 0.3h\ \mathrm{Mpc}^{-1}$ at $z = 1$.

Figure 9 summarizes the result of the MCMC analysis assuming an idealistically large survey with $V_s = 20h^{-3}\ \mathrm{Gpc}^3$. The two-dimensional contours of the 1-σ marginalized errors are shown for $D_A/D_{A,\mathrm{fid}}$ vs H/H_{fid} (bottom left), $D_A/D_{A,\mathrm{fid}}$ vs f (middle left), and f vs $D_A/D_{A,\mathrm{fid}}$ (bottom center). Also, the marginalized posterior distribution for each parameter is plotted in the top left, middle center, and bottom right panels. In each panel, blue and red lines, respectively, represent the results using the model of redshift distortion with and without the terms A and B.

As is clear from Fig. 9, the model including the corrections shows a better performance. Within the 1-σ errors, which roughly correspond to the precision of a percent level, it correctly reproduces the fiducial values of the parameters (indicated by crosses). On the other hand, the two-dimensional errors of the results neglecting the corrections show a clear evidence for the systematic bias on the best-fit parameters. Accordingly, the resultant value of

[3] In the case adopting linear galaxy bias, the growth-rate parameter f and the power spectra P_{ab} in the expression (18) are, respectively, replaced with $\beta \equiv f/b$ and b^2P_{ab}. Also, the standard PT expression for the corrections $A(k,\mu;f)$ and $B(k,\mu;f)$ should be replaced with $b^3\ A(k,\mu;\beta)$ and $b^4\ B(k,\mu;\beta)$.

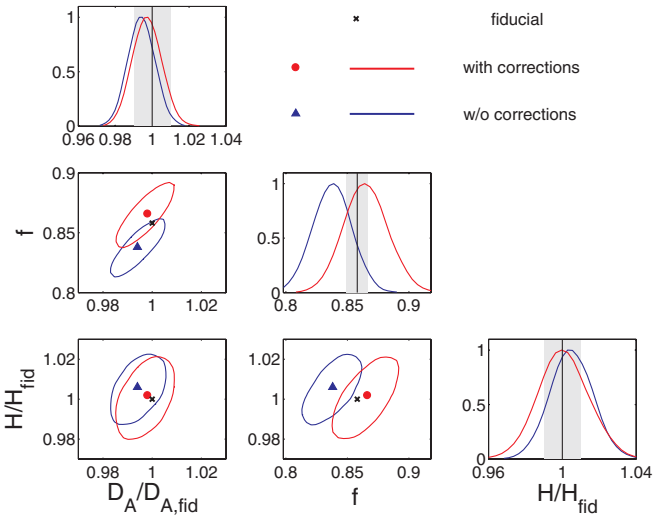

FIG. 9 (color online). Results of MCMC analysis using the model of redshift distortion with and without corrections (depicted as blue and red lines, respectively). Based on the power spectrum template (25), we derive the posterior distribution for the parameters D_A, H, and f from the monopole and quadrupole spectra of N-body simulations at $z = 1$, marginalized over the one-dimensional velocity dispersion σ_v and linear bias parameter b. Top left, middle center, and bottom right show the marginalized posterior distribution for $D_A/D_{A,\mathrm{fid}}$, H/H_{fid}, and f. Shaded regions indicate the 1% interval around the fiducial values. Middle left, bottom left, and bottom center plot the two-dimensional 1-σ errors on the surfaces $(H/H_{\mathrm{fid}}, f)$, $(D_A/D_{A,\mathrm{fid}}, H/H_{\mathrm{fid}})$, and $(f, H/H_{\mathrm{fid}})$. Note that in estimating the likelihood function (28), we adopted the linear theory to calculate the covariance matrix $\mathrm{Cov}_{\ell,\ell'}$, including the shot-noise contribution with $\bar{n}_g = 5 \times 10^{-4} h^3\ \mathrm{Mpc}^{-3}$ and assuming an idealistically large survey volume $V_s = 20 h^{-3}\ \mathrm{Gpc}^3$ (see Appendix C for an explicit expression).

χ^2 around the best-fit parameters, given by $\chi^2 = -2 \ln \mathcal{L}$, is larger than that of the case including the corrections $\chi^2 = 10.1$ and 22.2 for the cases with and without corrections, respectively. Although the deviation from the fiducial values seems somewhat small except for the growth-rate parameter f, this is solely due to the fact that we only use the monopole and quadrupole power spectra. It would be generally significant in the analysis using the full shape of the redshift-space power spectrum, for which the statistical errors are greatly reduced, and thereby the systematic biases would be prominent.

B. Impact of redshift distortion on future measurements of D_A, H, and f

Given the fact that the robust measurement of D_A, H, and f can be made with the new model of redshift distortion, we then move to the discussion on the potential impact on the future measurements using the *full shape* of the redshift-space power spectrum. Here, for illustrative purpose, we consider two surveys around $z = 1$, with volume $V_s = 4$ and $20 h^{-3}\ \mathrm{Gpc}^3$, and quantitatively estimate how the wrong model of redshift distortion leads to incorrect measurements of D_A, H, and f.

The fundamental basis to estimate the uncertainties and systematic biases on model parameters is the Fisher-matrix formalism. The Fisher matrix for a galaxy survey is given by

$$F_{ij} = \frac{V_s}{(2\pi)^2} \int_{k_{\mathrm{min}}}^{k_{\mathrm{max}}} dk k^2 \int_{-1}^{1} d\mu \frac{\partial \ln P^{(\mathrm{S})}_{\mathrm{obs}}(k,\mu)}{\partial p_i} \times \frac{\partial \ln P^{(\mathrm{S})}_{\mathrm{obs}}(k,\mu)}{\partial p_j} \left\{ \frac{\bar{n}_g P^{(\mathrm{S})}_{\mathrm{obs}}(k,\mu)}{\bar{n}_g P^{(\mathrm{S})}_{\mathrm{obs}}(k,\mu) + 1} \right\}^2 \tag{29}$$

with $\bar{n}_{\mathrm{gal}}$ being the number density of galaxies, for which we specifically set $\bar{n}_{\mathrm{gal}} = 5 \times 10^{-4} h^3\ \mathrm{Mpc}^{-3}$. The minimum wave number available for a given survey, k_{min}, is set to $2\pi/V_s^{1/3}$. Here, the observed power spectrum $P^{(\mathrm{S})}_{\mathrm{obs}}$ is given by Eq. (25), and we allow for the influence of galaxy biasing adopting the deterministic linear relation, $\delta_{\mathrm{gal}} = b\delta_{\mathrm{m}}$. Then, we have five parameters in total, given by $p_i = \{b, f, \sigma_v, D_A/D_{A,\mathrm{fid}}, H/H_{\mathrm{fid}}\}$. Fiducial values of these parameters are set as $b = 2$, $f = 0.858$, $D_A/D_{A,\mathrm{fid}} = 1$, and $H/H_{\mathrm{fid}} = 1$. As for the velocity dispersion σ_v, we use the fitted result to N-body simulations adopting the new model of redshift distortion in Sec. IV B, and set $\sigma_v = 395\ \mathrm{km\,s}^{-1}$.

Based on the Fisher matrix (29), the systematic bias for parameter p_i caused by incorrectly modeling the theoretical power spectrum is estimated from the following formula:

$$\Delta p_i = -\sum_j (F'^{-1})_{ij} s_j, \tag{30}$$

where F'^{-1} is the inverse Fisher matrix evaluated at the fiducial parameter set, but is obtained from an incorrect model of redshift distortion as a theoretical template of redshift-space power spectrum. The vector s_j is given by

$$s_j = \frac{V_s}{(2\pi)^2} \int dk k^2 \int_{-1}^{1} d\mu \frac{P^{\mathrm{sys}}(k,\mu)}{P^{\mathrm{wrong}}(k,\mu)} \frac{\partial \ln P^{\mathrm{wrong}}(k,\mu)}{\partial p_j} \times \left\{ \frac{\bar{n}_g P^{\mathrm{wrong}}(k,\mu)}{1 + \bar{n}_g P^{\mathrm{wrong}}(k,\mu)} \right\}^2. \tag{31}$$

The function $P^{\mathrm{wrong}}(k,\mu)$ is the theoretical template adopting the incorrect model of redshift distortion. The systematic differences in the power spectrum amplitude are quantified as $P^{\mathrm{sys}}(k,\mu) = P^{\mathrm{wrong}}(k,\mu) - P^{\mathrm{true}}(k,\mu)$, where $P^{\mathrm{true}}(k,\mu)$ is the correct template for the redshift-space power spectrum $P^{(\mathrm{S})}_{\mathrm{obs}}$, for which we assume the new model of redshift distortion including the terms A and B [Eq. (18)]. Below, we will quantify the magnitude of systematic biases if we incorrectly apply the model of redshift distortion neglecting the corrections A and B for the power spectrum template.

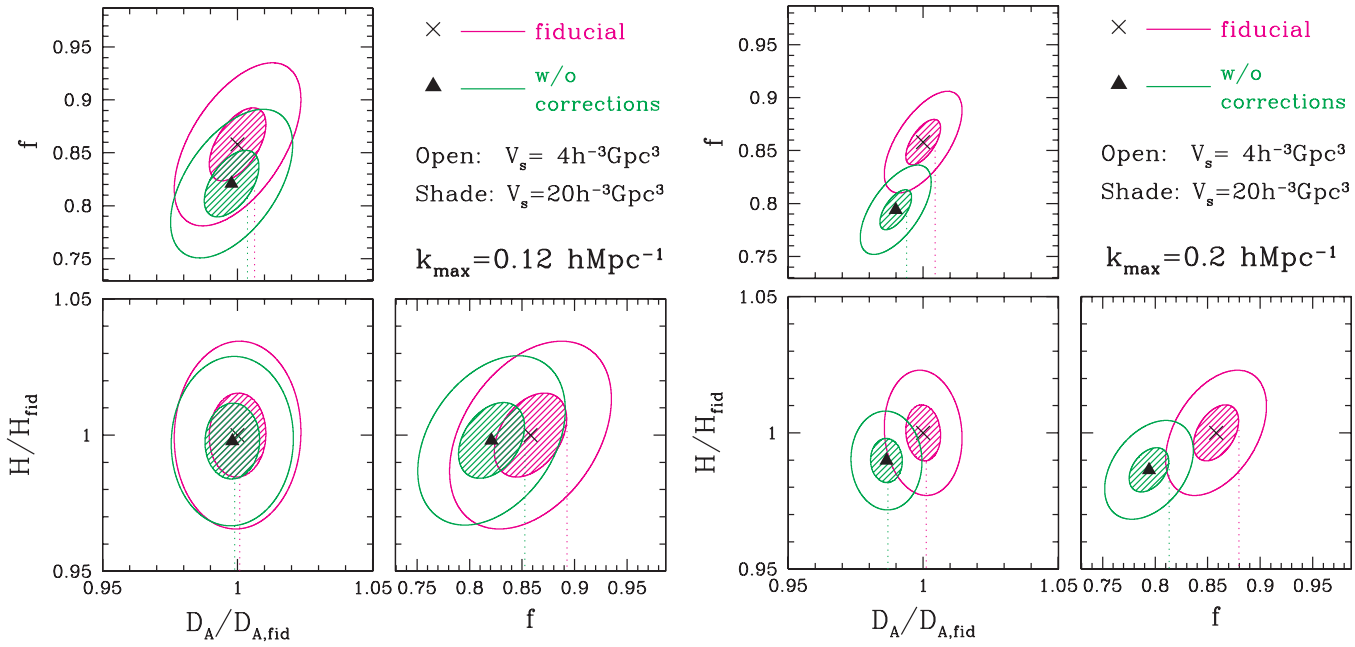

FIG. 10 (color online). Expected two-dimensional contours on marginalized errors around the best-fit values of $D_A/D_{A,\mathrm{fid}}$ vs H/H_{fid} (bottom left), f vs H/H_{fid} (bottom right) and $D_A/D_{A,\mathrm{fid}}$ vs f (top left) at $z = 1$, obtained from the *full shape* of the redshift-space power spectrum. The maximum wave number for parameter estimation is chosen as $k_{\mathrm{max}} = 0.12$ (left panels) and $0.2h$ Mpc^{-1} (right panels), so as to satisfy the condition $k_{\mathrm{max}} < k_{1\%}$ for standard PT and improved PT, respectively. In each panel, open and shaded contours indicate the two-dimensional errors for the surveys with $V_s = 4$ and $20h^{-3}$ Gpc^3.

Figure 10 plots the results of the Fisher-matrix calculations marginalized over the nuisance parameters b and σ_{v}. The uncertainties and biases for the best-fit values of f, D_A, and H are estimated assuming $k_{\mathrm{max}} = 0.12h$ Mpc^{-1} (left panel) and $0.2h$ Mpc^{-1} (right panel), and the results are shown for the surveys with $V_s = 4h^{-3}$ Gpc^3 (open) and $20h^{-3}$ Gpc^3 (shaded). In each panel, two-dimensional contours around the crosses and filled triangles show the expected 1-σ (68% C.L.) errors around the best-fit values adopting the model of redshift distortion with and without the corrections, respectively. The differences between best-fit values (crosses and filled triangles) represent the systematic biases estimated from Eq. (30), which remain unchanged irrespective of the survey volume V_s. Since the size of marginalized uncertainties is proportional to $V_s^{-1/2}$, the systematic bias in the best-fit parameters becomes relatively prominent and is considered to be a serious problem if we increase the survey volume. Note that similar to the result in Fig. 9, there exists a tight correlation between the growth-rate parameter f and quantities D_A and H. This is consistent with the finding by Ref. [58], indicating that distinguishing dark energy from modified gravity requires another observational constraint.

Figure 10 implies that the phenomenological model of redshift distortion neglecting the corrections can produce a large systematic error. By increasing the maximum wave number k_{max}, the bias on the measurements of angular diameter distance and Hubble parameter reaches $\sim$1%–2% error, while the best-fit value for the growth-rate parameter would be seriously biased with $\sim$5% error. If we conservatively choose a smaller value of $k_{\mathrm{max}} \lesssim 0.12h$ Mpc^{-1}, these systematics could still be within the statistical error for surveys with typical volume of $V_s \sim 4h^{-3}$ Gpc^3. However, for a survey of larger volume with $V_s \gtrsim 20h^{-3}$ Gpc^3, the systematic error on the growth-rate parameter exceeds the marginalized uncertainty. If we aggressively choose $k_{\mathrm{max}} \sim 0.2h$ Mpc^{-1} in order to reduce statistical uncertainties, the systematic biases become definitely serious issues in all of the parameters f, D_A, and H for both surveys of volume $V_s = 4$ and $20h^{-3}$ Gpc^3. Hence, correctly modeling redshift distortion would be very crucial for both stage-III and -IV class surveys defined by the Dark Energy Task Force [59].

VI. DISCUSSION AND CONCLUSION

In this paper, we have investigated the power spectrum in redshift space and presented a new model of redshift distortion, which is particularly suited for modeling anisotropic BAOs around $k = 0 \sim 0.3h$ Mpc^{-1}. Contrary to the previous phenomenological models in which the effects of Kaiser and Finger-of-God are separately treated in a multiplicative way, the new model includes the corrections coming from the nonlinear coupling between velocity and density fields, which give rise to a slight uplift in the amplitude of monopole and quadrupole power spectra. The

model predictions can give a good agreement with results of N-body simulations, and a percent-level precision is almost achieved.

Based on the new model of redshift distortion, we proceeded to the parameter estimation analysis and checked if the theoretical prediction correctly recovers the cosmological information from the monopole and quadrupole spectra of N-body simulations. MCMC analysis revealed that while the new model of redshift distortion combining the improved PT calculation faithfully reproduces the fiducial parameters D_A, H, and f and the precision can reach the percent level, the model neglecting the corrections (A and B terms) exhibits a slight offset of the best-fit values. In order to estimate the potential impact on future measurements, we have further made the Fisher-matrix analysis using the full shape of the power spectrum $P^{(S)}(k, \mu)$, and found that the existing phenomenological models of redshift distortion neglecting the corrections produce a systematic error on measurements of the angular diameter distance and Hubble parameter by 1%–2%, and the growth-rate parameter by $\sim$5%. This would become non-negligible for stage-III and -IV class surveys defined by the Dark Energy Task Force. Correctly modeling redshift distortion is thus crucial, and the new prescription for the redshift-space power spectrum presented here plays an essential role in constraining the dark energy and/or modified gravity from anisotropic BAOs.

Finally, we note several remaining tasks in practical application to the precision measurement of BAOs. One is the improved treatment for calculation of the corrections, A and B terms, which needs to evaluate the bispectrum of density and velocity fields. In doing this, a systematic treatment using a multipoint propagator developed by Ref. [60] would be useful and indispensable. Also, the effects of the new contributions to the redshift-space clustering in the presence of the primordial non-Gaussianity and the dark-sector interaction would be presumably important (e.g., [10,61,62]), and should deserve further investigation. Of course, the biggest issue is the galaxy biasing. Recent numerical and analytical studies claim that the scale-dependent and stochastic properties of the galaxy bias can change the redshift-space power spectrum, and the potential impact on the determination of the growth-rate parameter would be significant [63,64]. A realistic modeling of galaxy biasing relevant for the scale of BAOs is thus essential, and a further improvement of the power spectrum template needs to be developed.

ACKNOWLEDGMENTS

We would like to thank Yasushi Suto and Kazuhiro Yamamoto for comments and discussion, and Takahiko Matsubara for comments and teaching us the technique to derive the formula in Appendix B. We also thank Jordan Carlson for a careful reading of the manuscript. A. T. is supported by a Grant-in-Aid for Scientific Research from the Japan Society for the Promotion of Science (JSPS) (No. 21740168). T. N. and S. S. are supported by the JSPS. This work was supported in part by a Grant-in-Aid for Scientific Research on Priority Areas No. 467 "Probing the Dark Energy through an Extremely Wide and Deep Survey with Subaru Telescope," and the JSPS Core-to-Core Program "International Research Network for Dark Energy."

APPENDIX A: PERTURBATION THEORY CALCULATIONS FOR CORRECTION TERMS

In this Appendix, we present the perturbative expressions for the corrections A and B defined in Eqs. (19) and (20), which originate from the coupling between Kaiser and Finger-of-God effects.

Let us first consider the correction A, which involves the bispectrum B_σ of density and velocity divergence [see Eq. (21)]. Using the perturbative solutions up to the second order, the leading-order result of the bispectrum becomes

$$\begin{aligned} B_\sigma(\boldsymbol{k}_1, \boldsymbol{k}_2, \boldsymbol{k}_3) = (-2f)\Bigg[&\left(1 + \frac{k_{2z}^2}{k_2^2} f\right)\left(1 + \frac{k_{3z}^2}{k_3^2} f\right) G_2(\boldsymbol{k}_2, \boldsymbol{k}_3) P_{\rm lin}(k_2) P_{\rm lin}(P_3) \\ &+ \left(1 + \frac{k_{3z}^2}{k_3^2} f\right)\left\{F_2(\boldsymbol{k}_1, \boldsymbol{k}_3) + \frac{k_{2z}^2}{k_2^2} f G_2(\boldsymbol{k}_1, \boldsymbol{k}_3)\right\} P_{\rm lin}(k_1) P_{\rm lin}(P_3) \\ &+ \left(1 + \frac{k_{2z}^2}{k_2^2} f\right)\left\{F_2(\boldsymbol{k}_1, \boldsymbol{k}_2) + \frac{k_{3z}^2}{k_3^2} f G_2(\boldsymbol{k}_1, \boldsymbol{k}_2)\right\} P_{\rm lin}(k_1) P_{\rm lin}(P_2)\Bigg] \end{aligned} \tag{A1}$$

with F_2 and G_2 being the second-order perturbation kernels given by (e.g., [22,26,65])

$$F_2(\boldsymbol{k}_1, \boldsymbol{k}_2) = \frac{5}{7} + \frac{\boldsymbol{k}_1 \cdot \boldsymbol{k}_2}{2 k_1 k_2}\left(\frac{k_1}{k_2} + \frac{k_2}{k_1}\right) + \frac{2}{7}\left(\frac{\boldsymbol{k}_1 \cdot \boldsymbol{k}_2}{k_1 k_2}\right)^2, \qquad G_2(\boldsymbol{k}_1, \boldsymbol{k}_2) = \frac{3}{7} + \frac{\boldsymbol{k}_1 \cdot \boldsymbol{k}_2}{2 k_1 k_2}\left(\frac{k_1}{k_2} + \frac{k_2}{k_1}\right) + \frac{4}{7}\left(\frac{\boldsymbol{k}_1 \cdot \boldsymbol{k}_2}{k_1 k_2}\right)^2.$$

Note that the bispectrum (A1) possesses the following symmetries: $B_\sigma(\boldsymbol{k}_1, \boldsymbol{k}_2, \boldsymbol{k}_3) = B_\sigma(\boldsymbol{k}_1, \boldsymbol{k}_3, \boldsymbol{k}_2) = B_\sigma(-\boldsymbol{k}_1, -\boldsymbol{k}_2, -\boldsymbol{k}_3)$. Then, substituting the expression (A1) into the definition (19), the correction A can be recast schematically in the form as

$$A(k,\mu) = -k\mu \sum_{m,n} \int \frac{d^3\boldsymbol{p}}{(2\pi)^3} f^m p_z^n Q_{mn}(\boldsymbol{k},\boldsymbol{p}), \qquad \text{(A2)}$$

where the function Q_{mn} is the scalar function of $\boldsymbol{k}$ and $\boldsymbol{p}$. To further perform the angular integral, we use the formulas presented in Appendix B [Eq. (B3)], which can be obtained by utilizing the rotational covariance of the integral (see also Ref. [29]). After straightforward but lengthy calculation, the correction $A(k,\mu)$ is finally reduced to the following form:

$$A(k,\mu;z) = \sum_{m,n=1}^{3} \mu^{2m} f^n \frac{k^3}{(2\pi)^2} \Big[\int_0^\infty dr \int_{-1}^{+1} dx \{A_{mn}(r,x) P_{\rm lin}(k;z) + \tilde{A}_{mn}(r,x) P_{\rm lin}(kr;z)\} \frac{P_{\rm lin}(k\sqrt{1+r^2-2rx};z)}{(1+r^2-2rx)^2} + P_{\rm lin}(k;z) \int_0^\infty dr a_{mn}(r) P_{\rm lin}(kr;z) \Big], \qquad \text{(A3)}$$

where we introduce the quantities $r = k/p$ and $x = (\boldsymbol{k}\cdot\boldsymbol{p})/k/p$. Note again that μ is the cosine of the angle between line-of-sight direction $\hat{z}$ and the vector $\boldsymbol{k}$, i.e., $\mu = (\boldsymbol{k}\cdot\hat{z})/k$. The nonvanishing components of A_{mn}, $\tilde{A}_{mn}$, and a_{mn} are

$$A_{11} = -\frac{r^3}{7}\{x + 6x^3 + r^2x(-3+10x^2) + r(-3+x^2-12x^4)\}, \qquad A_{12} = \frac{r^4}{14}(x^2-1)(-1+7rx-6x^2),$$
$$A_{22} = \frac{r^3}{14}\{r^2x(13-41x^2) - 4(x+6x^3) + r(5+9x^2+42x^4)\}, \qquad A_{23} = A_{12},$$
$$A_{33} = \frac{r^3}{14}(1-7rx+6x^2)\{-2x + r(-1+3x^2)\},$$

for A_{mn},

$$\tilde{A}_{11} = \frac{1}{7}(x+r-2rx^2)(3r+7x-10rx^2), \qquad \tilde{A}_{12} = \frac{r}{14}(x^2-1)(3r+7x-10rx^2),$$
$$\tilde{A}_{22} = \frac{1}{14}\{28x^2 + rx(25-81x^2) + r^2(1-27x^2+54x^4)\}, \qquad \tilde{A}_{23} = \frac{r}{14}(1-x^2)(r-7x+6rx^2),$$
$$\tilde{A}_{33} = \frac{1}{14}(r-7x+6rx^2)(-2x-r+3rx^2),$$

for $\tilde{A}_{mn}$, and

$$a_{11} = -\frac{1}{84r}\Big[2r(19-24r^2+9r^4) - 9(r^2-1)^3 \log\Big|\frac{r+1}{r-1}\Big|\Big],$$
$$a_{12} = \frac{1}{112r^3}\Big[2r(r^2+1)(3-14r^2+3r^4) - 3(r^2-1)^4 \log\Big|\frac{r+1}{r-1}\Big|\Big],$$
$$a_{22} = \frac{1}{336r^3}\Big[2r(9-185r^2+159r^4-63r^6) + 9(r^2-1)^3(7r^2+1)\log\Big|\frac{r+1}{r-1}\Big|\Big], \qquad a_{23} = a_{12},$$
$$a_{33} = \frac{1}{336r^3}\Big[2r(9-109r^2+63r^4-27r^6) + 9(r^2-1)^3(3r^2+1)\log\Big|\frac{r+1}{r-1}\Big|\Big].$$

for a_{mn}.

Next consider the corrections B. This term is already of the order $\mathcal{O}(\{P_{\rm lin}(k)\}^2)$, and the nonvanishing contribution can be estimated without employing the perturbative calculations. Just applying the formula (B3) in Appendix B to Eq. (20), we obtain

$$B(k,\mu) = \sum_{n=1}^{4}\sum_{a,b=1}^{2} \mu^{2n}(-f)^{a+b} \frac{k^3}{(2\pi)^2} \int_0^\infty dr \int_{-1}^{+1} dx B_{ab}^n(r,x) \frac{P_{a2}(k\sqrt{1+r^2-2rx}) P_{b2}(kr)}{(1+r^2-2rx)^a}, \qquad \text{(A4)}$$

where $P_{12}(k) = P_{\delta\theta}(k)$ and $P_{22}(k) = P_{\theta\theta}(k)$. The nonvanishing coefficients B_{ab}^n are

$$B^1_{11} = \frac{r^2}{2}(x^2-1), \qquad B^1_{12} = \frac{3r^2}{8}(x^2-1)^2, \qquad B^1_{21} = \frac{3r^4}{8}(x^2-1)^2, \qquad B^1_{22} = \frac{5r^4}{16}(x^2-1)^3,$$

$$B^2_{11} = \frac{r}{2}(r+2x-3rx^2), \qquad B^2_{12} = -\frac{3r}{4}(x^2-1)(-r-2x+5rx^2), \qquad B^2_{21} = \frac{3r^2}{4}(x^2-1)(-2+r^2+6rx-5r^2x^2),$$

$$B^2_{22} = -\frac{3r^2}{16}(x^2-1)^2(6-30rx-5r^2+35r^2x^2), \qquad B^3_{12} = \frac{r}{8}\{4x(3-5x^2)+r(3-30x^2+35x^4)\},$$

$$B^3_{21} = \frac{r}{8}[-8x+r\{-12+36x^2+12rx(3-5x^2)+r^2(3-30x^2+35x^4)\}],$$

$$B^3_{22} = \frac{3r}{16}(x^2-1)[-8x+r\{-12+60x^2+20rx(3-7x^2)+5r^2(1-14x^2+21x^4)\}],$$

$$B^4_{22} = \frac{r}{16}[8x(-3+5x^2)-6r(3-30x^2+35x^4)+6r^2x(15-70x^2+63x^4)+r^3\{5-21x^2(5-15x^2+11x^4)\}].$$

The expression (A4) is still nonperturbative in the sense that we do not perturbatively treat the power spectra $P_{\delta\theta}$ and $P_{\theta\theta}$ in the integrand. For the leading-order calculation, we simply apply the linear-theory calculation to these quantities, and replace both $P_{\delta\theta}$ and $P_{\theta\theta}$ with the linear spectrum $P_{\rm lin}$.

Codes for computing the corrections A and B, together with the standard and improved PT calculations for $P_{\delta\delta}$, $P_{\delta\theta}$, and $P_{\theta\theta}$, are available upon request.

APPENDIX B: SOME USEFUL FORMULAS FOR INTEGRALS

In this Appendix, we give the integral formulas used in Appendix A to derive the perturbative expressions for the correction A and B. A brief sketch of the derivation can also be found in Ref. [29] (see Appendix A and B of this paper).

Let us first consider the integral of an arbitrary scalar function $f(\boldsymbol{k}, \boldsymbol{p})$ times some vectors over $\boldsymbol{p}$. A simple example of the integrand is $p_i p_j f(\boldsymbol{k}, \boldsymbol{p})$, where subscripts i, j select the x, y, or z direction. The rotationally invariant properties of the integral implies that the resultant form of the integral is given by

$$\int \frac{d^3\boldsymbol{p}}{(2\pi)^3} p_i p_j f(\boldsymbol{k}, \boldsymbol{p}) = P\delta_{ij} + Qk_ik_j, \tag{B1}$$

irrespective of the functional form of $f(\boldsymbol{k}, \boldsymbol{p})$. The coefficients P and Q are obtained by contracting the above integral with δ_{ij} and k_ik_j, and are functions of $k = |\boldsymbol{k}|$. We have

$$P = \frac{k^5}{(2\pi)^2}\int dr r^2 \int_{-1}^{1} dx x \frac{r^2}{2}(1-x^2) f(k, r, x),$$

$$Q = \frac{k^3}{(2\pi)^2}\int dr r^2 \int_{-1}^{1} dx x \frac{r^2}{2}(3x^2-1) f(k, r, x),$$

where we write $p = kr$ and $\boldsymbol{k}\cdot\boldsymbol{p} = k^2 rx$. Thus, as a special case with $i = j = z$, we get the following formula:

$$\int \frac{d^3\boldsymbol{p}}{(2\pi)^3} p_z^2 f(\boldsymbol{k}, \boldsymbol{p}) = P + (k\mu)^2 Q \tag{B2}$$

with $k_z = k\mu$.

The above procedure can be generalized to the cases of integrals involving arbitrary numbers of multiplicative vectors. As a useful formula, we here explicitly write down the result summing up the integrals of arbitrary scalar functions f_n times the power p_z^n up to the sixth order:

$$\sum_{n=0}^{6}\int \frac{d^3\boldsymbol{p}}{(2\pi)^3} p_z^n f_n(\boldsymbol{k}, \boldsymbol{p}) = \frac{k^3}{(2\pi)^2}\sum_{m,n=0}^{6}\mu^n \int_0^\infty dr r^2 \int_{-1}^{+1} dx (kr)^m G_{nm}(x) f_m(k, r, x). \tag{B3}$$

The nonvanishing coefficients G_{nm} as functions of k, r, and x are summarized as follows:

$$G_{00} = 1, \quad G_{02} = -\frac{1}{2}(x^2-1), \quad G_{04} = \frac{3}{8}(x^2-1)^2, \quad G_{06} = -\frac{5}{16}(x^2-1)^3, \quad G_{11} = x,$$
$$G_{13} = -\frac{3}{2}x(x^2-1), \quad G_{15} = \frac{15}{8}x(x^2-1)^2, \quad G_{22} = \frac{1}{2}(3x^2-1), \quad G_{24} = -\frac{3}{4}(5x^4-6x^2+1),$$
$$G_{26} = \frac{15}{16}(7x^2-1)(x^2-1)^2, \quad G_{33} = \frac{1}{2}x(5x^2-3), \quad G_{35} = -\frac{5}{4}x(7x^4-10x^2+3),$$
$$G_{44} = \frac{1}{8}(35x^4-30x^2+3), \quad G_{46} = \frac{15}{16}(-21x^6+35x^4-15x^2+1), \quad G_{55} = \frac{1}{8}(63x^4-70x^2+15),$$
$$G_{66} = \frac{1}{16}(231x^6-315x^4+105x^2-5).$$

APPENDIX C: COVARIANCE BETWEEN MULTIPOLE POWER SPECTRA

Here, we give the explicit expression for covariance between multipole power spectra used in the MCMC analysis in Sec. VA.

Neglecting the non-Gaussian contribution, the nonvanishing part of the covariance only appears in the diagonal components (i.e., correlation between the same Fourier modes), which are expressed as (e.g., Refs. [66,67])

$$\mathrm{Cov}_{\ell,\ell'}(k) = \frac{2}{N_k}\frac{(2\ell+1)(2\ell'+1)}{2}\int_{-1}^{1} d\mu \mathcal{P}_\ell(\mu)\mathcal{P}_{\ell'}(\mu) \times \left\{P^{(\mathrm{S})}(k,\mu) + \frac{1}{\bar{n}_\mathrm{g}}\right\}^2, \tag{C1}$$

where N_k is the number of Fourier modes within a given bin at k, given by $N_k = 4\pi k^2 \Delta k/(2\pi/V_s^{1/3})^3$ with Δk and V_s being the bin width and survey volume, respectively.

For an analytic estimate of the covariance, we assume that the power spectrum is simply written as $P^{(\mathrm{S})}(k,\mu) = (1+\beta\mu^2)^2 b^2 P_\mathrm{lin}(k)$, where b is the linear bias parameter and β is defined by $\beta \equiv f/b$. Substituting this into Eq. (C1), we obtain

$$\mathrm{Cov}_{0,0}(k) = \frac{2}{N_k}\left[\left(1+\frac{4}{3}\beta+\frac{6}{5}\beta^2+\frac{4}{7}\beta^3+\frac{1}{9}\beta^4\right) \times \{b^2P_\mathrm{lin}(k)\}^2 + \frac{2}{\bar{n}_\mathrm{g}}\left(1+\frac{2}{3}\beta+\frac{1}{5}\beta^2\right) \times b^2P_\mathrm{lin}(k) + \frac{1}{\bar{n}_\mathrm{g}^2}\right] \tag{C2}$$

for $(\ell,\ell') = (0,0)$,

$$\mathrm{Cov}_{0,2}(k) = \frac{2}{N_k}\left[\left(\frac{8}{3}\beta+\frac{24}{7}\beta^2+\frac{40}{21}\beta^3+\frac{40}{99}\beta^4\right) \times \{b^2P_\mathrm{lin}(k)\}^2 + \frac{2}{\bar{n}_\mathrm{g}}\left(\frac{4}{3}\beta+\frac{4}{7}\beta^2\right)b^2P_\mathrm{lin}(k)\right] \tag{C3}$$

for $(\ell,\ell') = (0,2)$ or (2,0), and

$$\mathrm{Cov}_{2,2}(k) = \frac{2}{N_k}\left[\left(5+\frac{220}{21}\beta+\frac{90}{7}\beta^2 + \frac{1700}{231}\beta^3+\frac{2075}{1287}\beta^4\right)\{b^2P_\mathrm{lin}(k)\}^2 + \frac{2}{\bar{n}_\mathrm{g}}\left(5+\frac{220}{21}\beta+\frac{30}{7}\beta^2\right)b^2P_\mathrm{lin}(k) + \frac{5}{\bar{n}_\mathrm{g}^2}\right] \tag{C4}$$

for $(\ell,\ell') = (2,2)$.

[1] A. J. S. Hamilton, in *The Evolving Universe*, edited by D. Hamilton (Kluwer Academic, Dordrecht, The Netherlands, 1998), pp. 185–275.
[2] P. Peebles, *The Large-Scale Structure of The Universe* (Princeton University Press, Princeton, NJ, 1980).
[3] A. J. S. Hamilton, Astrophys. J. **385**, L5 (1992).
[4] S. Cole, K. B. Fisher, and D. H. Weinberg, Mon. Not. R. Astron. Soc. **267**, 785 (1994).
[5] E. V. Linder, Astropart. Phys. **29**, 336 (2008).
[6] L. Guzzo *et al.*, Nature (London) **451**, 541 (2008).
[7] K. Yamamoto, T. Sato, and G. Huetsi, Prog. Theor. Phys. **120**, 609 (2008).

[8] Y.-S. Song and W. J. Percival, J. Cosmol. Astropart. Phys. 10 (2009) 004.
[9] Y.-S. Song and I. Kayo, arXiv:1003.2420.
[10] K. Koyama, R. Maartens, and Y.-S. Song, J. Cosmol. Astropart. Phys. 10 (2009) 017.
[11] W. Zimdahl and D. Pavon, Phys. Lett. B **521**, 133 (2001).
[12] G. R. Farrar and P. J. E. Peebles, Astrophys. J. **604**, 1 (2004).
[13] C. Alcock and B. Paczynski, Nature (London) **281**, 358 (1979).
[14] H.-J. Seo and D. J. Eisenstein, Astrophys. J. **598**, 720 (2003).
[15] C. Blake and K. Glazebrook, Astrophys. J. **594**, 665 (2003).
[16] K. Glazebrook and C. Blake, Astrophys. J. **631**, 1 (2005).
[17] M. Shoji, D. Jeong, and E. Komatsu, Astrophys. J. **693**, 1404 (2009).
[18] N. Padmanabhan and M. J. White, Phys. Rev. D **77**, 123540 (2008).
[19] B. A. Reid *et al.*, Mon. Not. R. Astron. Soc. **404**, 60 (2010).
[20] W. J. Percival *et al.*, Mon. Not. R. Astron. Soc. **401**, 2148 (2010).
[21] E. A. Kazin, M. R. Blanton, R. Scoccimarro, C. K. McBride, and A. A. Berlind, Astrophys. J. **719**, 1032 (2010).
[22] F. Bernardeau, S. Colombi, E. Gaztanaga, and R. Scoccimarro, Phys. Rep. **367**, 1 (2002).
[23] D. Jeong and E. Komatsu, Astrophys. J. **651**, 619 (2006).
[24] D. Jeong and E. Komatsu, Astrophys. J. **691**, 569 (2009).
[25] T. Nishimichi *et al.*, Publ. Astron. Soc. Jpn. **61**, 321 (2009).
[26] M. Crocce and R. Scoccimarro, Phys. Rev. D **73**, 063519 (2006).
[27] M. Crocce and R. Scoccimarro, Phys. Rev. D **73**, 063520 (2006).
[28] M. Crocce and R. Scoccimarro, Phys. Rev. D **77**, 023533 (2008).
[29] T. Matsubara, Phys. Rev. D **77**, 063530 (2008).
[30] T. Matsubara, Phys. Rev. D **78**, 083519 (2008).
[31] P. McDonald, Phys. Rev. D **75**, 043514 (2007).
[32] K. Izumi and J. Soda, Phys. Rev. D **76**, 083517 (2007).
[33] A. Taruya and T. Hiramatsu, Astrophys. J. **674**, 617 (2008).
[34] A. Taruya, T. Nishimichi, S. Saito, and T. Hiramatsu, Phys. Rev. D **80**, 123503 (2009).
[35] M. Pietroni, J. Cosmol. Astropart. Phys. 10 (2008) 036.
[36] S. Matarrese and M. Pietroni, J. Cosmol. Astropart. Phys. 06 (2007) 026.
[37] P. Valageas, Astron. Astrophys. **421**, 23 (2004).
[38] P. Valageas, Astron. Astrophys. **465**, 725 (2007).
[39] E. Komatsu *et al.* (WMAP Collaboration), Astrophys. J. Suppl. Ser. **180**, 330 (2009).
[40] M. Crocce, S. Pueblas, and R. Scoccimarro, Mon. Not. R. Astron. Soc. **373**, 369 (2006).
[41] V. Springel, Mon. Not. R. Astron. Soc. **364**, 1105 (2005).
[42] R. Scoccimarro, Phys. Rev. D **70**, 083007 (2004).
[43] N. Kaiser, Mon. Not. R. Astron. Soc. **227**, 1 (1987).
[44] J. C. Jackson, Mon. Not. R. Astron. Soc. **156**, 1P (1972).
[45] M. Davis and P. J. E. Peebles, Astrophys. J. **267**, 465 (1983).
[46] A. F. Heavens, S. Matarrese, and L. Verde, Mon. Not. R. Astron. Soc. **301**, 797 (1998).
[47] D. J. Eisenstein and W. Hu, Astrophys. J. **496**, 605 (1998).
[48] J. Carlson, M. White, and N. Padmanabhan, Phys. Rev. D **80**, 043531 (2009).
[49] W. J. Percival and M. White, Mon. Not. R. Astron. Soc. **393**, 297 (2009).
[50] S. Cole, K. B. Fisher, and D. H. Weinberg, Mon. Not. R. Astron. Soc. **275**, 515 (1995).
[51] J. A. Peacock and S. J. Dodds, Mon. Not. R. Astron. Soc. **267**, 1020 (1994).
[52] C. Park, M. S. Vogeley, M. J. Geller, and J. P. Huchra, Astrophys. J. **431**, 569 (1994).
[53] W. E. Ballinger, J. A. Peacock, and A. F. Heavens, Mon. Not. R. Astron. Soc. **282**, 877 (1996).
[54] H. Magira, Y. P. Jing, and Y. Suto, Astrophys. J. **528**, 30 (2000).
[55] R. Takahashi *et al.*, Mon. Not. R. Astron. Soc. **389**, 1675 (2008).
[56] A. Lewis and S. Bridle, Phys. Rev. D **66**, 103511 (2002).
[57] R. Takahashi *et al.*, Astrophys. J. **700**, 479 (2009).
[58] F. Simpson and J. A. Peacock, Phys. Rev. D **81**, 043512 (2010).
[59] A. J. Albrecht *et al.*, arXiv:astro-ph/0609591.
[60] F. Bernardeau, M. Crocce, and R. Scoccimarro, Phys. Rev. D **78**, 103521 (2008).
[61] F. Schmidt, Phys. Rev. D **82**, 063001 (2010).
[62] F. Simpson, B. M. Jackson, and J. A. Peacock, arXiv:1004.1920.
[63] V. Desjacques and R. K. Sheth, Phys. Rev. D **81**, 023526 (2010).
[64] T. Okumura and Y. P. Jing, arXiv:1004.3548.
[65] T. Nishimichi *et al.*, Publ. Astron. Soc. Jpn. **59**, 1049 (2007).
[66] K. Yamamoto, Astrophys. J. **595**, 577 (2003).
[67] K. Yamamoto, M. Nakamichi, A. Kamino, B. A. Bassett, and H. Nishioka, Publ. Astron. Soc. Jpn. **58**, 93 (2006).